Renewable and Sustainable Energy Reviews 88 (2018) 16–36

Contents lists available at ScienceDirect

Renewable and Sustainable Energy Reviews

journal homepage: www.elsevier.com/locate/rser

A review of foundations of offshore wind energy convertors: Current status and future perspectives

Ki-Yong Oh[a,1], Woochul Nam[b,1], Moo Sung Ryu[c], Ji-Young Kim[c], Bogdan I. Epureanu[b,*]

[a] School of Energy Systems Engineering, Chung-Ang University, 84 Heukseok-ro, Dongjak-gu, Seoul 06974, Republic of Korea
[b] Scho ol of Mechanical Engineering, Chung-Ang University, 84, Heukseuk-ro, Dongjack-gu, Seoul 06974, Republic of Korea
[c] Renewable Energy Group, Korea Electric Power Corporation Research Institute, Munjiro 105, Yuseong-gu, Daejeon 34056, Republic of Korea

ARTICLE INFO

Keywords:
Offshore foundations
Offshore wind energy convertors
Offshore wind turbines
Structure-soil interaction

ABSTRACT

This paper reviews foundations for offshore wind energy convertors considering the significant growth of offshore wind energy since the early 2000s. The characteristics of various foundation types (i.e., gravity, pile, suction caisson, and float type) and the current status of field application are discussed. Moreover, the mechanical characteristics of soil are described in the sense that these characteristics including modulus, strength, damping, and modulus degradation of soil play critical roles for the design of offshore foundations. By using these mechanical properties of soil, theoretical studies to consider structure-soil interaction are classified (into equivalent spring models, distributed spring models, and continuous element models) and explained. Field and laboratory experiments on the response of structure embedded in soil to static and dynamic loads are discussed. Based on the review of previous studies, directions for future research and study on offshore wind turbine are suggested.

1. Introduction

The development of renewable and sustainable energy sources not only mitigates concerns regarding the volatility of oil prices and the emission of carbon dioxide but also reduces the dependency of energy on fossil fuels. Wind energy is one of the promising solutions for sustainable energy because of its maturity and comparatively low cost [1].

In particular, offshore wind power can be a primary energy source in the future considering the high-energy density, lower turbulence, lower wind shear, and fewer civil complaints compared to onshore wind power. Total cumulative capacity in the offshore wind energy converters (OWECs) rose to 8759 MW in 2014 (Fig. 1). Large-scale offshore wind farms have been constructed in Europe, and their power production accounts for more than 90% of power generated by all OWECs. Total capacity has increased to 8.0 GW in 74 offshore wind farms in 11 European countries in 2014. Approximately, 1.5 GW of offshore wind was installed in 2014 [1]. Moreover, dozens of GW-capacity offshore wind farms are scheduled to be constructed over the next decades [2–4].

The United Kingdom (UK) and Germany lead the development of large-scale commercial offshore wind farms. China has become the third largest annual market in 2014. The Chinese government also announced a list of 44 future offshore projects with capacity of 10.53 GW [1]. Several pilot projects and commercial developments have been concurrently conducted in Taiwan, Japan, and South Korea [5,6]. Indeed, wind is a major source of power along with nuclear and fossil fuel (coal) energies, and its share is increasing significantly (Fig. 1).

Technological advances constantly improve the economic feasibility of offshore wind farms. For example, Round I offshore farms in the UK had an average monthly capacity factor of 33.6%, while Round 2 offshore farms increased their average monthly capacity factor to 38.3% [7]. However, many challenges facing the growth of offshore wind farms still remain. Specifically, the construction costs of offshore wind farms are 1.5–2 times greater than that of onshore wind farms [8] because offshore wind farms require expensive foundations, installation, and grid connections (e.g., underwater cabling and offshore transformer stations).

Especially, the cost for a foundation of an OWEC increases depending upon water depth (Fig. 2). The cost of OWEC foundations is about 20% of their total cost, and 45% of the wind turbine cost in shallow water depth. The cost for foundations at the water depth of 40–50 m is 1.9 times higher than the cost for the water depth of 10–20 m. Therefore, selecting a suitable OWEC foundation type and

* Corresponding author.
E-mail address: epureanu@umich.edu (B.I. Epureanu).
[1] These authors contributed equally to this paper.

https://doi.org/10.1016/j.rser.2018.02.005
Received 29 April 2016; Received in revised form 20 February 2017; Accepted 14 February 2018

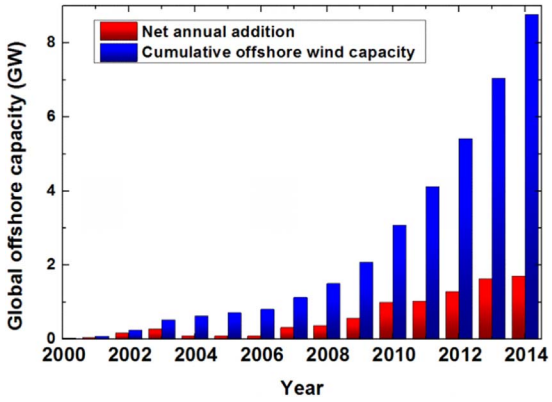

Fig. 1. Global offshore wind power capacity from 2000 to 2014; left bars show the net annual addition each year, while right bars represent cumulative offshore wind capacity every year; data used in this figure is from [1,3].

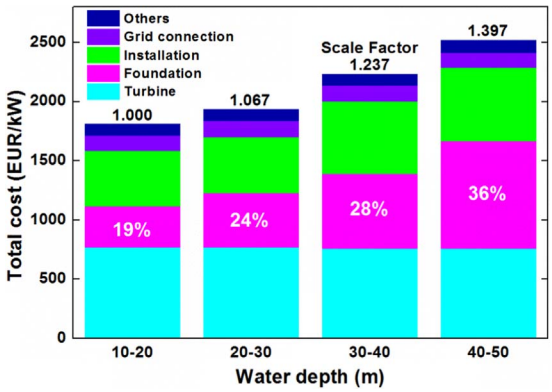

Fig. 2. Cost breakdown of offshore wind farm over water depth; data used in this figure is from [9].

optimally designing it are the most important factors to lower the cost.

Designing foundations for OWECs is more difficult than designing offshore oil and gas platforms. Aerodynamic loads acting on OWECs are significant because of their large blade span. Oil and gas offshore platforms are designed to minimize aerodynamic loads. However, large aerodynamic loads are unavoidable to OWECs because both rotational and thrust forces are applied to their turbine blades. This large aerodynamic load causes significant moments on the foundation of OWECs because the large loads act on the nacelles which are located at the top of the long wind turbine towers. Therefore, the large aerodynamic loads and their interaction with hydrodynamic loads need to be considered to prevent fatigue and failure of the structure. Hydrodynamic loads acting on OWECs and oil (or gas) platforms are also different. OWECs are installed in shallow and transient waters, whereas oil platforms are mainly installed in deep waters. The effect of sediment movement and scour on offshore structures depends upon these conditions. These differences suggest that optimization techniques, design methods, and field experience obtained from oil and gas foundations cannot be directly applied to the design of OWECs and substructures. Thus, intensive efforts in both theory and experiment are required.

This review of foundations of OWECs is aimed for a broad spectrum of readers from academia, research, and industry. The text covers a broad spectrum of topics from basic knowledge to the state-of-the-art research including research perspectives, challenges, and future trends. Section 2 describes basic concepts and future trends of various foundations for commercial OWECs in operation, which might be useful for researchers who wish to catch up quickly with the current state of foundations for large-scale offshore wind farms. The pros, cons and limits of each type of foundation are also explained for the same reason. Section 3 presents the fundamental characteristics of soils. This section includes the dynamic behavior of soils needed for the analysis of structure-soil interaction and the degradation behavior of soils needed for fatigue analysis. Also, we provide basic knowledge about the dynamic and static behaviors of soils over short- and long-term period, which is essential to design OWECs and their foundation and to predict the structural response of OWECs. Material properties of various soils are also listed for readers who need these properties for their studies. Note that understanding the nature of soils should be preceded to design foundations of OWECs because soils play critical roles for the behavior and response of OWECs. Section 4 discusses the principles, current states, and future challenges of modeling methods for structure-soil interaction. Research on modeling methods are categorized into three different model types: equivalent spring models, distributed springs models, and continuum element models. Various experiments on the structure-soil interaction are also discussed because that interaction is highly nonlinear. There experimental observations provide valuable information to develop new modeling methods and to suggest parameters used in modeling. Moreover, modeling and experimental efforts for suction caisson type of foundation are emphasized in a separate section. This type of foundation is the most promising in the future because it is accompanied with relatively small vibration, noise, and suspended sediments during installation [10]. Nonetheless, this type of foundation still faces challenges, which are also described in this section. Lastly, Section 5 suggests future research trends and challenges for the design of foundations of OWECs from several perspectives to secure the safety and reliability of offshore wind farms.

2. Types of foundation

The sea depth is generally classified into three classes: shallow waters (0–30 m), transitional waters (30–50 m), and deep waters (50–200 m) [11,13]. The sea depth is the most important factor for the viability of offshore wind farms because the cost for foundations significantly increases over the depth. Hence, several types of foundations are already developed, and some types are under development considering the sea depth and other conditions (Fig. 3).

Fig. 4(a) shows the current types of foundations used in commercial OWECs with respect to the sea depth and the distance from shore. This figure, which contains reorganized data from Tables 1–3, provides insights into trends for foundation types with respect to the sea depth and the distance from shore (Table 4).

In shallow waters, gravity type (Fig. 3(a)) and monopile type foundations (Fig. 3(b)) are mainly used. Initial offshore wind farms adopted these two types because their reliability is ensured in shallow waters. Especially, the monopile type is most frequently used because of the sea depth at available farm locations and the capacity of installed OWECs. The gravity type is not used for OWECs over 3 MW (Fig. 4(b)) because it has to be very heavy and expensive to be constructed in deeper seas, with depths over 10 m, in order to resist high aero- and hydro- dynamic loads for high capacity of wind turbine.

In transitional and deep waters, a monopile type and a multipod type are mainly deployed. Note that values corresponding to multipod include both tripod and jacket. This observation is also related to the capacity of OWECs. As OWECs with higher capacity, over 5 MW, have been installed in deeper waters, over 30 m, multipod type foundations have been selected to lower costs.

Fig. 4 also shows the trend of foundations for OWECs over the sea depth and the capacity: gravity – monopile – multipod. As the site is deeper and is farther from shore, multipod is more widely used than gravity and monopile foundations because of high economic feasibility. Note that floating type foundations are not included in Fig. 4 because most OWECs with floating type foundations are demo versions. The test floating OWEC foundations target very deep sites (e.g., 100–200 m) and have high rated capacity (e.g., 5–6 MW) [37,38,41]. The current status of applications for different foundations are discussed in the following sub-sections.

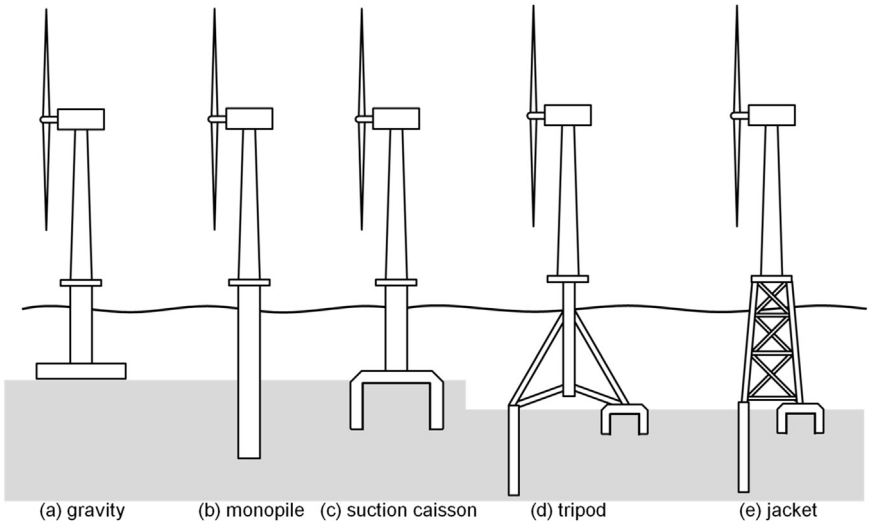

Fig. 3. Types of foundations for OWECs.

2.1. Gravity

A gravity-type foundation, which consists of a large circular pile with a concrete plate structure resting on the seabed, is historically the first type of foundations deployed for OWECs (Fig. 3(a)). Gravity is the main source to keep the structure upright. The detailed procedure for construction is described in [12]. Initial offshore wind farms in Denmark were installed by using this type of foundation close to shore, where the water depth is very shallow, as listed in Table 1. Moreover, several demonstration projects such as the Avedøre Holme, Breitling, Thornton Bank (Phase I) offshore wind farms used this type of foundation because this mature construction and installation technology can minimize risk.

2.2. Monopile

This type of foundations is mainly used for most OWECs, especially in European offshore wind farms (Table 2) for the following reasons. First, most European offshore wind farms have been constructed in shallow waters with less than 30 m depth. Second, the soil in the North Sea mainly consists of sand and gravel, which requires relatively less effort on drilling of piles. This technology is the most economical solution so far considering seabed conditions in Europe. Ninety-one percent of offshore wind farms, which were fully grid connected in 2014, also adopted this foundation type [3]. More details for the monopile foundation are provided in [13].

Several studies on monopile foundations suggested that this foundation type can reduce material costs while maintaining performance [23,24]. However, this technology requires heavy duty equipment like jack-up barges for installation, which cause considerable vibration, noise, and suspended sediment. Hence, fisheries and other environmental issues should be considered for installing offshore wind farms with this substructure.

2.3. Suction caisson

A suction caisson replicating an upside down bucket (Fig. 3(c)) is an eco-friendly foundation because it does not need heavy equipment for piling. This is beneficial to installation due to its low level of vibration, noise, and suspended sediment. Moreover, this type of foundations is economic because of the simple and fast installation procedure [13]. Specifically, a 3.0 MW OWEC was installed with a prototype suction caisson at Frederikshavn in 2002 for the first time, showing that the suction caisson reduces the steel weight by half compared with a traditional monopile [25]. The Korea Electric Power Corporation Research Institute (KEPCO RI) also constructed two offshore metrological masts with different types of substructures. The first Herald of Meteorological and Oceanographic Special research Unit (HeMOSU-1) adopted a jacket piles substructure, whereas HeMOSU-2 addressed the tripod suction caisson foundation [27,28] (Fig. 5). The cost analysis for HeMOSU-2 confirmed that the tripod suction caisson foundation requires half of the construction cost compared to jacket piles for the same seabed geology

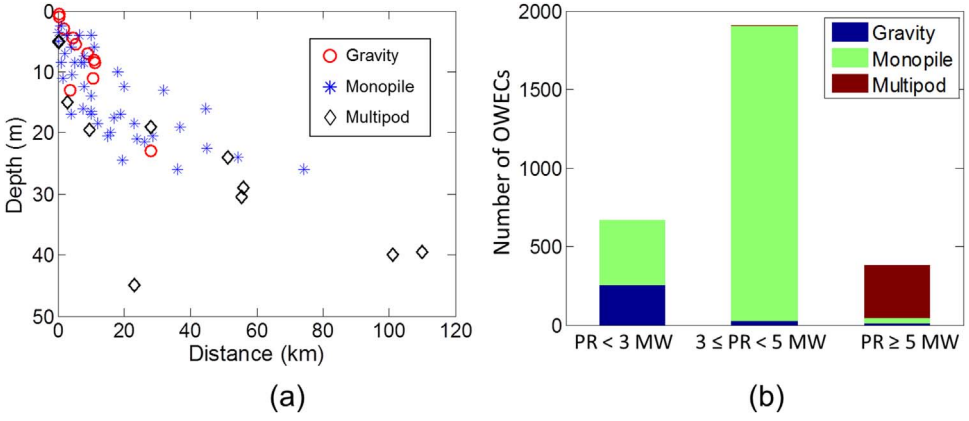

Fig. 4. Comparisons of installed foundations for OWECs; symbols in figure (a) represent wind farms constructed with each foundation type; bars in figure (b) represent the number of OWECs with respect to the capacity of OWECs (Power Rating, PR).

Table 1
Offshore wind farms constructed with gravity type foundations [14–22].

Wind farm	Turbine	Rating (MW)	# of WTs	Total capacity (MW)	Depth (m)	Distance to shore (km)	Location[a]
Avedøre Holme	SWP-3.6-120	3.6	3	11	0–2	0.4	D
Middelgrunden	Bonus B76	2.0	20	40	3–6	4.7	D
Nysted (Rødsand I)	SWP-2.3-82	2.3	72	166	6–10	11	D
Rødsand II	SWP-2.3-93	2.3	90	207	4–10	9	D
Sprogø	Vestas V90	3.0	7	21	6–16	10.6	D
Tunø Knob	Vestas V39	0.5	10	5	4–7	5.5	D
Vindeby	Bonus 450 kW	0.45	11	5	2–4	1.8	D
Breitling	Nordex N90	2.5	1	2.5	0.5	0.3	G
Karehamn	Vestas V112	3.0	16	48	6–20	3.8	S
Lillgrund	SWT-2.3-93	2.3	48	110	4–13	11.3	S
Thornton Bank (Phase I)	Repower 5M	5.0	6	30	18–28	28	B

[a] B: Belgium, D: Denmark, G: Germany, S: Sweden.

[28]. Remarkably, the penetration of HeMOSU-2 with the tripod suction caisson foundation was completed in 6 h, while HeMOSU-1 spent two months for the installation. This suggests that suction caissons are excellent solutions from construction and installation perspectives. However, it is unclear whether suction caissons are suitable for OWECs at sites with transitional water depth considering the significant aerodynamic and hydrodynamic loads exerted on OWECs. Therefore, KEPCO RI is conducting a demonstration project entitled Seashore wind tUrbine Construction & Commercialization Embedded Suction bucket Support structure (SUCCESS) to establish the design criteria for a substructure with suction caissons.

Table 2
Offshore wind farms constructed with monopile type foundations [14–22].

Wind farm	Turbine	Rating (MW)	# of WTs	Total capacity (MW)	Depth (m)	Distance to shore (km)	Location[a]
Anholt	SWP-3.6-120	3.6	111	400	15–19	15–23	D
Horns Rev I	V80	2.0	80	160	6–14	18	D
Horns Rev II	SWP-2.3-93	2.3	91	209	9–17	32	D
Samsø	SWP-2.3-82	2.3	10	23	14–20	4	D
Amrumbank West	SWP-3.6-120	3.6	80	288	20–25	44.8	G
DanTysk	SWP-3.6-120	3.6	80	288	21–31	74.3	G
EnBW Baltic 1	SWP-2.3-93	2.3	21	48	16–19	17.1	G
Meerwind Süd/Ost	SWT-3.6-120	3.6	80	288	22–26	54.4	G
Riffgat	SWT-3.6-120	3.6	30	108	18–23	15–42	G
Egmond aan Zee	V90	3.0	36	108	15–18	10	N
Eneco Luchterduinen	V112	3.0	43	129	18–24	24	N
Irene Vorrink	NTK600-43	0.6	28	17	2–3	1	N
Lely	Nedwind-41	0.5	4	2	3–4	0	N
Princess Amalia	V80	2.0	60	120	19–24	26	N
Bockstigen	WinWorld	0.55	5	3	6	4	S
Utgrunden	Enron 70	1.5	7	11	6–15	4.2	S
Yttre Stengrund	NM 72	2.0	5	10	6–8	2	S
Belwind	V90	3.0	55	165	12–20	44.7	B
Northwind	V112	3.0	72	216	15–23	37	B
Kamisu – phase 1	Subaru 80	2.0	7	14	5	0.2	J
Kamisu – phase 2	HTW 2.0-80	2.0	8	16	5	0.1	J
Barrow	Vestas V90	3.0	30	90	12–20	7.5	UK
Blyth Offshore	Vestas V66	2.0	2	4	6–11	1	UK
Burbo Bank	SWT-3.6-107	3.6	25	90	0–8	6.4	UK
Greater Gabbard	SWP-3.6-107	3.6	140	504	20–32	36	UK
Gunfleet Sands 1 & 2	SWP-3.6-107	3.6	48	173	2–15	7	UK
Gunfleet Sands 3 (Demonstration)	SWP-6.0-120	6.0	2	12	5–12	8	UK
Gwynt y Môr	SWP-3.6-107	3.6	160	576	12–28	16	UK
Humber Gateway	V112	3.0	73	219	10–18	10	UK
Kentish Flats	V90	3.0	30	90	3–5	10	UK
Lincs	SWP-3.6-120	3.6	75	270	10–15	8	UK
London Array	SWP-3.6-120	3.6	175	630	0–25	20	UK
Lynn and Inner Dowsing	SWP-3.6-107	3.6	54	194	6–11	5	UK
North Hoyle	Vestas V80	2.0	30	60	5–12	7	UK
Rhyl Flats	SWP-3.6-107	3.6	25	90	4–11	8	UK
Robin Rigg	V90	3.0	60	180	0–12	11	UK
Scroby Sands	Vestas V80	2.0	30	60	0–8	2.5	UK
Sheringham Shoal	SWP-3.6-107	3.6	88	317	14–23	23	UK
Teesside	SWT-2.3-93	2.3	27	62	7–15	1.5	UK
Thanet	V90	3.0	100	300	14–23	12	UK
Walney	SWP-3.6-107	3.6	102	367	19–30	14	UK
West of Duddon Sands	SWP-3.6-120	3.6	108	389	17–24	15	UK
Westermost Rough	SWP-6.0-154	6.0	35	210	12–22	10	UK

[a] B: Belgium, D: Denmark, G: Germany, J: Japan, N: Netherlands, S: Sweden, UK: United Kingdom.

Table 3
Offshore wind farms constructed with tripod or jacket type foundations [14–22].

Wind farm	Turbine	Rating (MW)	# of WTs	Total capacity (MW)	Depth (m)	Distance to shore (km)	Type[a]	Location[b]
Alpha Ventus	Areva M5000 REpower 5M	5.0	12	60	28–30	56	T J	G
BARD Offshore 1	BARD 5.0	5.0	80	400	39–41	101	T	G
Global Tech I	Areva M116	5.0	80	400	38–41	110	T	G
Hooksiel	Bard 5.0	5.0	1	5	5	0.4	T	G
Nordsee Ost	Senvion 126	6.2	48	298	22–26	51.4	J	G
Trianel Windpark Borkum (Phase 1)	Areva M116	5.0	40	200	28–33	45–66	T	G
Thornton Bank phase II & III	Senvion 126	6.15	48	295	12–26	28.2	J	B
Jeju Island (Demonstration)	STX 72 WinDS3000	2.0 3.0	2	5	15	2.8	J	K
Beatrice (Demonstration)	Repower	5.0	2	10	45	23	J	UK
Methil	Samsung	7.0	1	7	5	0.05	J	UK
Ormonde	Repower	5.0	30	150	17–22	9.5	J	UK

[a] J: Jacket, T: Tripod.
[b] B: Belgium, G: Germany, K: Korea, UK: United Kingdom.

Table 4
Soil classification in terms of grain size and corresponding properties [42].

Material		Compactness	Dr (%)	N	γ_d (kN/m^3)	e	ϕ (°)
GW	Well-graded gravel, grave-sand mixture	Dense	75	90	22.1	0.22	40
		Medium dense	50	55	20.8	0.28	36
		Loose	25	< 28	19.7	0.36	32
GP	Poorly grade gravels, gravel sand mixtures	Dense	75	70	20.4	0.33	38
		Medium dense	50	50	19.2	0.39	35
		Loose	25	< 20	18.3	0.47	32
SW	Well-graded sands, gravelly sands	Dense	75	65	18.9	0.43	37
		Medium dense	50	35	17.9	0.49	34
		Loose	25	< 15	17.0	0.57	30
SP	Poorly graded sands, gravelly sand	Dense	75	50	17.6	0.52	36
		Medium dense	50	30	16.7	0.60	33
		Loose	25	< 10	15.9	0.65	29
SM	Silty sands	Dense	75	45	16.5	0.62	35
		Medium dense	50	25	15.6	0.74	32
		Loose	25	< 8	14.9	0.80	29
ML	Inorganic silts, fine sands	Dense	75	35	14.9	0.0	33
		Medium dense	50	20	14.1	0.90	31
		Loose	25	< 4	13.5	1.0	27

2.4. Multipod (tripod and jacket)

Different concepts of substructures are needed to lower construction costs for transitional water depth. Space frame substructures such as tripod and jacket structures can provide the required strength and stiffness (Fig. 3(d) and (e)). Tripod and jacket structures provide sufficient bearing capacity in transitional water depths with relative short penetration length. Moreover, the relatively low weight of tripods and jackets enhance the economic feasibility. The Alpha Ventus and Beatrice demonstration projects encourage the development of offshore wind farms with this substructure in transitional water depth, as listed in Table 3. More details for the multipod foundation are provided in [13].

These concepts are also suitable for the Korean peninsula considering the water depth and meteorological characteristics. Most feasible sites featuring high wind potential for large-scale development are in water deeper than 20 m [26]. Moreover, multipod can be more effective than monopod. If monopods are adopted, longer piles or larger suction caissons are required for extreme events such as hurricanes and typhoons. The design optimization of a structure is important for a multipod type foundation because the design of this foundation type is relatively complicated [29,30].

Fig. 5. Offshore meteorological masts with different types of substructures in the yellow sea of Korean Peninsula.

2.5. Floating

Floating structures have many advantages in deep waters in cost, construction, installation, and decommission. Moreover, technologies developed for the oil and gas industry provide valuable information, even though several differences exist because of different aero- and hydro-dynamic load characteristics of OWECs. This type is classified into three classes in terms of how the design achieves its stability: ballast stabilized, mooring line stabilized (tension leg platform), and buoyancy stabilized foundations [13,31,32]. Details for each design are described in [31,33,40].

StatoilHydro, oil and gas company in Norway, has been developed the ballast stabilized foundations [38]. Intensive numerical dynamic analysis of integrated systems, model scale tests, and full scale tests with a 2.3 MW wind turbine are conducted in the Hywind project. This project verified that ballast stabilized foundations are reliable [34–37]. StatoilHydro is preparing for the 30 MW pilot project consisting of five 6 MW floating turbines with the ballast stabilized foundation to show the economic feasibility, safety, and reliability of this concept for commercial development [38]. Oceanwind Technology (floating platform developer) proposed an economical layout of offshore wind farms with ballast stabilized foundations [39]. Floating units are arranged with a certain geometrical pattern by using cables. The number of anchors to maintain the positions of OWECs is minimized in the project.

The National Renewable Energy Laboratory (NREL) mainly studied the tension leg platform in cooperation with Massachusetts Institute of Technology [40]. They have been focused on the design of a floating structure with mooring lines [40]. Considering the relatively lower cost of this floating structure for the installation, this type is the most promising foundation among floating platforms.

A stabilized barge is mainly used for the buoyancy stabilized foundation. The stabilized barge is connected to the seabed by using anchors. Stabilizing an excessive gyroscopic motion under extreme wave conditions is the most significant challenge for this foundation. NREL conducted several studies with this foundation [31,40], and showed that vibrations along the yaw and the translational directions can be reduced significantly by controlling the pitch angle of the blades. In the first phase of the Fukushima floating offshore wind farm demonstration project, the semi-submersible platform with a 2 MW wind turbine was constructed [41]. In the second phase, 5 MW and 7 MW wind turbines with advanced spars (ballast stabilized concept) and V-shape semisub (buoyancy stabilized concept) will be installed at the coast of Fukushima. This project is expected to provide valuable information regarding floating substructures of OWECs for future commercial farms.

3. Important features of soil dynamics for offshore wind turbine foundations

3.1. Soil properties and classifications

Soil properties including the shear modulus, Poisson's ratio, and shear strength are important to study the response of offshore structures. Hunt [42] presents soil properties for various grain size and compactness (Table 4). Dr, N, γ_d, ϕ, and e denote the average relative density, an empirical cone factor, unit weight for zero water content, internal friction angle, and void ratio (= the volume fraction between voids and grains). Soils also can be classified into cohesionless soil and cohesion soil (Table 5). γ_{sub} represents the unit weight when soil is saturated with water, and S_u denotes the undrained shear strength.

In general, soils have different properties over depth. Thus, several properties of soils can be estimated over depth by performing in situ tests such as the cone penetration test (CPT) and the standard penetration test (SPT). The CPT can identify bearing resistance, friction resistance, and pore water pressure. Soil samples collected through the SPT can be used to estimate properties of soil such as soil classification and Poisson's ratio. In the SUCCESS project, the CPT and the SPT were carried out to characterize the soil properties over seabed depth at the location of HeMOSU-2, and the values are provided in Table 6.

Table 5
Soil properties for cohesionless soils and cohesive soils [43].

● cohesionless soils			
Soil type, compactness & consistency	γ_d (kN/m^3)	γ_{sub} (kN/m^3)	ϕ (°)
Loose gravel with low sand content	16–19	6–9	28–30
Medium dense gravel with low sand content	18–20	8–10	30–36
Dense to very dense gravel with low sand content	19–21	9–11	36–46
Loose well-graded sandy gravel	18–20	8–10	28–30
Medium-dense well-graded sandy gravel	19–21	9–11	30–36
Dense well graded sandy gravel	20–22	10–12	36–45
Loose clayey sandy gravel	18–20	8–10	28–30
Medium-dense clayey sandy gravel	19–21	9–11	30–35
Dense to very dense clayey sandy gravel	21–22	11–12	35–40
Loose coarse to fine sand	17–20	7–10	28–30
Medium-dense coarse to fine sand	20–21	10–11	30–35
Dense to very dense coarse to fine sand	21–22	11–12	35–40
Loose fine and silty sand	15–17	5–7	28–30
Medium-dense fine and silty sand	17–19	7–9	30–35
Dens to very dense fine and silty sand	19–21	9–11	35–40
● cohesive and organic soils			
Soil type, compactness & consistency	γ_d (kN/m^3)	γ_{sat} (kN/m^3)	S_u (kPa)
Soft plastic clay	16–19	6–9	20–40
Firm Plastic clay	17.5–20	7.5–10	40–75
Stiff plastic clay	18–21	8–11	75–150
Soft slightly plastic clay	17–20	7–10	20–40
Firm slightly plastic clay	18–21	8–11	40–750
Stiff slightly plastic clay	21–22	11–12	75–150
Stiff to very stiff clay	20–23	10–13	150–300
Organic clay	14–17	4–7	–
Peat	10.5–14	0.5–4	–

Table 6
Soil properties over depth for the location of HeMOSU-2; averaged values for each layer of soil are provided.

Depth (m)	Soil type	γ_d (kN/m^3)	S_u (kPa)	ϕ (°)	ν
0.0–12.0	Lean clay	18	11	26	0.40
12.0–26.3	Silty sand	19	27	33	0.36
26.6–27.5	Poorly-graded sand	20	–	35	0.35
27.5–30.3	Lean clay	19	50	–	0.35
30.3–39.0	Poorly-graded sand	20	–	35	0.35
39.0–42.0	Lean clay	19	50	–	0.35
42.0–46.0	Weathered soil	19	30	30	0.33
46.0–49.5	Weathered rock	21	36	32	0.31

3.2. Shear modulus and Poisson's ratio

The shear modulus of soils varies upon the depth and the type of loading (static or dynamic) and on the magnitude of the dynamic loading. The effects of the dynamic loading on the soil modulus can be classified into three different cases depending on the level of applied shear strain [44–46] (Fig. 6(a)). The values of the two thresholds for the shear strain (i.e., the linear cyclic threshold shear strain γ_{tl} and the volumetric cyclic threshold shear strain γ_{tv}) over various types of soils were well organized by Rodriguez et al. [46]. The dashed-arrow curve in Fig. 6(a) shows the expected range of shear strain for an installed foundation [45]. Because both hysteresis and degradation of modulus play a critical role in this range, they should be considered for OWECs.

In the very small strain regime, the soil can be considered to be a linear elastic material and does not exhibit hysteric damping. The shear modulus is not affected by the cycling strains in this regime. The shear modulus for this very small strains is referred to as the initial tangent

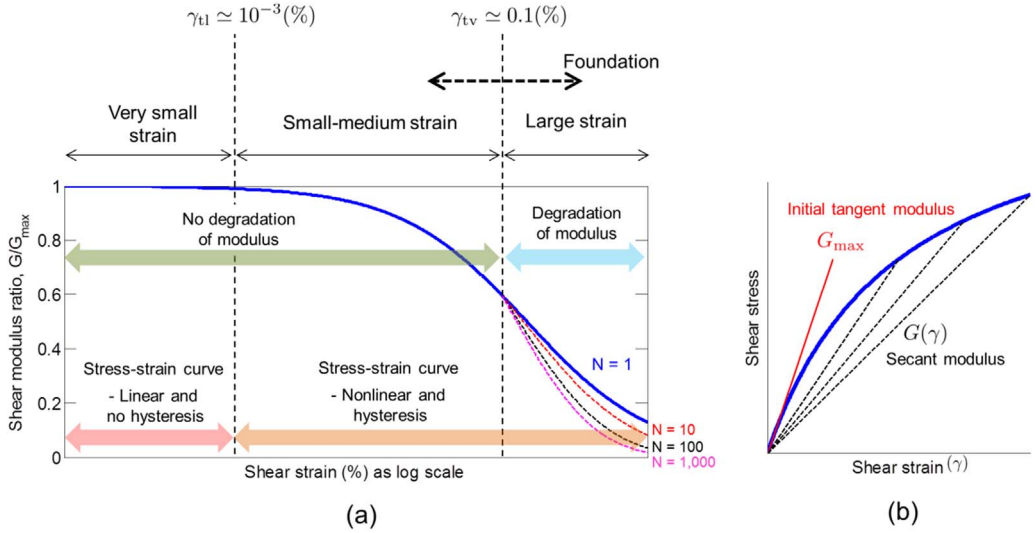

Fig. 6. Shear modulus of soil as a function of shear strain.

modulus (G_{max}) which can be obtained in the stress-strain curve, as shown in Fig. 6(b). The initial tangent shear modulus can be calculated by using a formula proposed by Hardin et al. [47,48],

$$G_{max} = 625\frac{OCR^k}{0.3 + 0.7e^2}(P_a\sigma'_m)^{\alpha}, \quad (1)$$

where OCR is the overconsolidation ratio; P_a is the atmospheric pressure; and σ'_m is the mean effective stress which is equal to $(\sigma'_v + 2\sigma'_h)/3$. σ'_v is the vertical effective stress acting on the soil, and σ'_h is the horizontal effective stress. The value of exponent k depends on the plasticity index (PI). The value of k is equal to 0, 0.18, 0.31, 0.41, and 0.48, corresponding to the PI values of 0, 20, 40, 60, and 80, respectively. When the PI is equal to or larger than 100, the value of 0.5 can be used for k. For the exponent α, the value of 0.5 is used in Eq. (1). However, a chart of empirical equations for G_{max} presented in [45] shows that the value of α ranges between 0.4 and 0.6 depending on the void ratio e.

In the small-medium strain regime, the shear modulus is not constant over the magnitude of strain. The shear stress shows a nonlinear dependence on the shear strain. Moreover, the pore pressure is not accumulated over undrained cyclic loading or volume change for drained conditions [49–57]. The secant shear modulus (i.e., G which is described in Fig. 6(b)) decreases as the magnitude of shear strain increases. Vucetic et al. [44] created shear strain-secant shear modulus curves for various values of the PI based on previous experimental results (Fig. 7). The secant shear modulus and strain can be related by using the hyperbolic model presented in Eq. (2) [51].

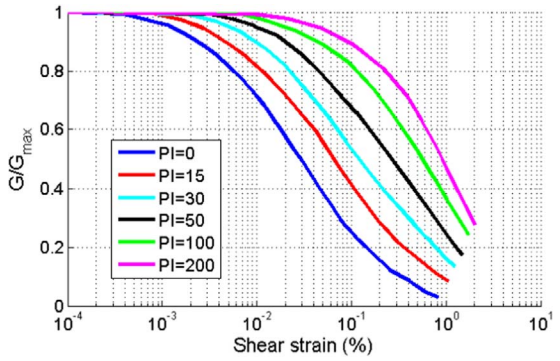

Fig. 7. Changes in the shear modulus over shear strain and PI.

$$\frac{G}{G_{max}} = \frac{1}{1+\gamma/\gamma_a}, \quad (2)$$

Where γ_a denotes the reference strain, which is the ratio between τ_{max} and G_{max}. τ_{max} denotes the ultimate shear resistance of the soil. The values of parameter γ_a are 0.028, 0.064, 0.1291, 0.2582, 0.5316, and 0.8849 corresponding to PI = 0, 15, 30, 50, 100, and 200, respectively. It is worthy to note that vertical (static) stress can also affect the modulus. When a soil is compressed by large vertical static loads, the change in the shear modulus over the strain is reduced in experiments with sand [50,58,59]. In this small-medium strain regime, stress-strain curve starts to generate hysteresis loops, which can be considered by using the extended Masing rule [60]. However, the value of modulus is not affected by the cyclic loads. The volumetric cyclic threshold strain γ_{tv} is a representative metric to distinguish small-strain and medium-strain regimes (where the modulus and hysteresis loop are the same over cycles) from the large-strain regime (where the modulus changes over cycle).

In the large shear strain regime, the nonlinearity in the shear modulus is stronger than that in the small-medium strain regime. Moreover, the shear modulus degrades over cycles for cyclic loads, because of changes in the microstructure of the soil. The degradation of shear modulus due to cyclic loads is presented in details in Section 3.5.

The shear modulus increases over the depth due to the compressive loads caused by the weight of the soil. The effects of the depth on the shear modulus can be estimated by using Eq. (1) which relates the vertical and horizontal effective stress to the shear modulus. The vertical effective stress σ'_v at a depth z can be calculated by integrating the submerged unit weights from 0 to z, where the submerged unit weight or effective unit weight denotes the unit weight of soil excluding the unit weight of water between soil grains. If the submerged unit weight is uniform over the soil, σ'_v is linearly proportional to z. The horizontal effective stress σ'_h can be related to the vertical effective stress with the lateral earth pressure coefficient K as $\sigma'_h = K\sigma'_v$. Thus, the mean effective stress σ'_m linearly increases over the depth z. By substituting the effects of the depth on the mean effective stress into Eq. (1) and by assuming that the changes of OCR and void ratio e over the depth are negligible, one can obtain the initial tangent shear modulus profile as

$$G_{max}(z) = Az^{\alpha}, \quad (3)$$

where α is the exponent in Eq. (1). Its value is about 0.5. The value of $G_{max}(z)$ over the depth was measured in various in situ experiments [45,61–67]. Fig. 8 presents the measured initial tangent shear modulus over the depth at several sites. The circles denote the measured initial

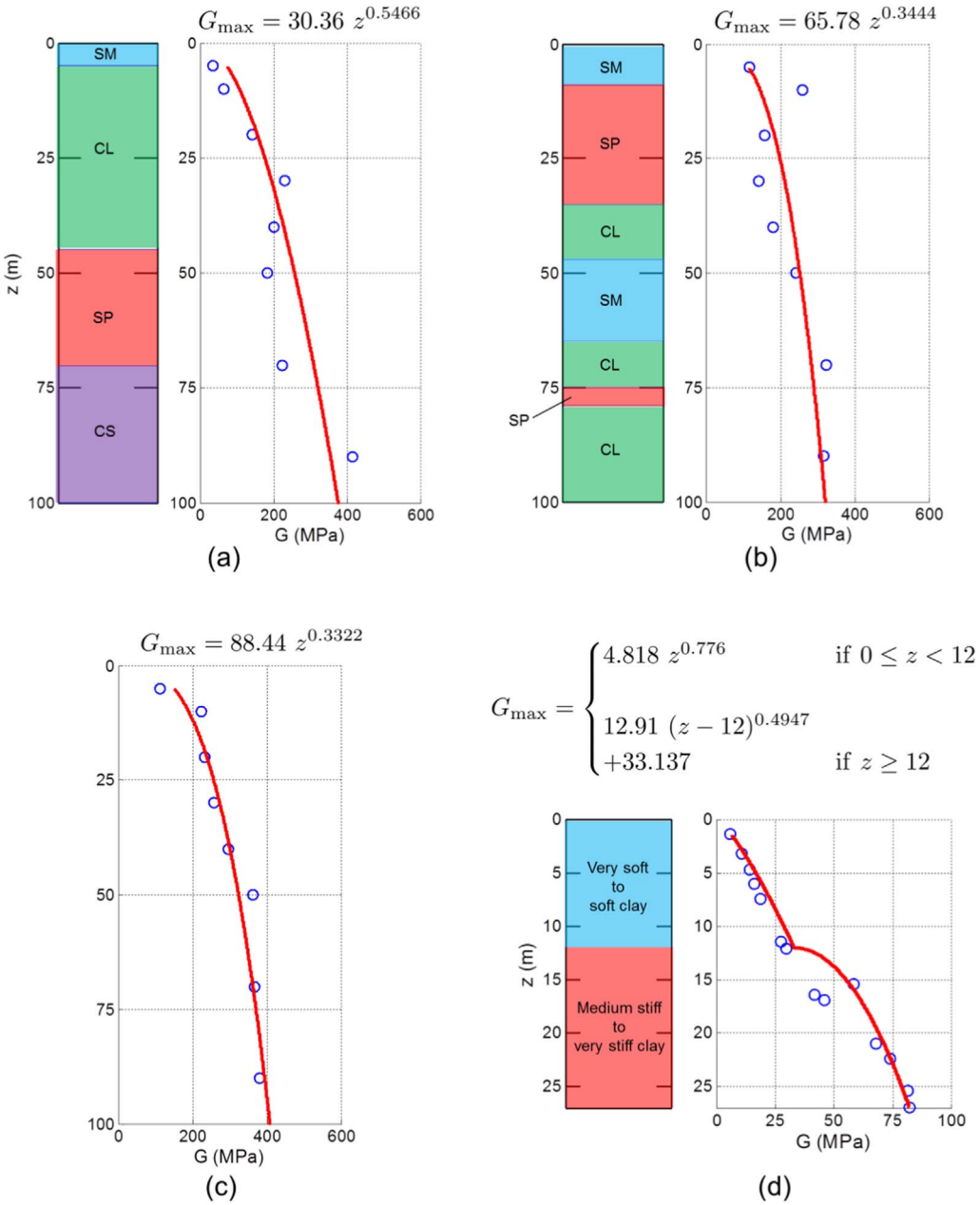

Fig. 8. In situ soil types and initial shear modulus G_{max} over the depth at several sites; New Jersey coast AMCOR 6010 (a) and 6009 (b), George's Bank (c), and Bangkok clays (d). This figure is created with data provided in [45,62,65].

shear modulus, and curves represent the shear modulus profiles generated by using Eq. (3). Fig. 8(a) and (b) show the initial shear modulus profiles of the New Jersey coast, AMCOR 6010 and 6009 [62,65]. The initial shear modulus profile in Fig. 8(c) corresponds to the profile of George's Bank [65], and Fig. 8(d) shows the profile of Bangkok clays [45]. Because Eq. (3) provides acceptable modulus profile, as shown in Fig. 8(a)–(c), it has been used in several studies [68–70]. However, it is difficult to estimate the modulus with Eq. (3) near boundaries between soil layers because different types of soils are mixed together in those regions. For example, the discrepancy between measured data and fitted profiles is shown around $z = 10$ m in Fig. 8(b) and around $z = 12$ m in Fig. 8(d). Note that the initial shear modulus in Fig. 8(d) changes significantly near $z = 12$ m where the soil type is changed. This change can be considered by using different values of A and α, as presented in the equation of Fig. 8(d). When the soil exhibits dramatic changes in soil properties (e.g., OCR, void ratio, PI, etc.) over the depth, it is necessary to use A of Eq. (3) as a function of OCR, void ratio e, and PI, instead of using a constant value.

The shear modulus of soils over the depth can be estimated by conducting in situ experiments such as the CPT and the SPT. Young's modulus (E) of soils can be calculated using its correlation to the SPT N-values, the cone tip bearing resistance q_c, or the undrained shear strength S_u. Several useful empirical equations for E are provided in Table 7. The shear modulus can be calculated by generating shear wave in soil and by measuring its density ρ and velocity $V_s$of shear wave traveling through soil [61]. Then, the value of shear modulus can be obtained as

$$G_{max}(z) = \rho V_s^2. \quad (4)$$

The Poisson's ratio of the soil is required to predict the mechanical response of soil for two or three dimensional finite element analysis. The value of the Poisson's ratio varies over the soil type; ν is 0.3–0.4 for sand, and 0.4–0.5 for clay [71,72]. The change in the Poisson's ratio over strain and over the depth is not considerable. Yokota et al. [71]

Table 7
Empirical equations used in the estimation of the modulus of elasticity (E_s) [74–77].

Soil type	SPT	CPT
Sand (normally Consolidated)	E_s = 500 (N + 15) E_s = (15000–22000) $\log_e$ N	E_s = (2–4) q_c
Sand (saturated)	E_s = 250 (N + 15)	–
Sand (over-consolidated)	E_s = 18000 + 750N	E_s = (6–30) q_c
Gravelly sand and gravel	E_s = 1200 (N + 6) E_s = 600 (N + 6) for N < 15 E_s = 600 (N + 6) for N > 15	–
Clayey sand	E_s = 320 (N + 15)	E_s = (3–6) q_c
Silty sand	E_s = 300 (N + 6)	E_s = (1–2) q_c
Soft clay	–	E_s = (3–8) q_c
Clay (Plastic index > 30)	E_s = (100–500) S_u	–
Clay (Plastic index < 30)	E_s = (500–1500) S_u	–
Clay (OCR > 2)	E_s = (1500–2000) S_u	–

showed that the changes of the Poisson's ratio in the range of shear strain 0.01–1% are very small. Also, the Poisson's ratio change over the depth is only 0.03 over 150 m [72]. When the ground is composed of various soil layers, the Poisson's ratio is not significantly affected by the depth [73]. However, the water content of soil strongly affects the Poisson's ratio. The Poisson's ratio of sand is about 0.4 for a large water content (i.e., around 40%) [71]. However, if the water content changes to only 20% due to the confining pressure, the Poisson's ratio of sand is reduced to 0.25.

3.3. Shear strength

The shear strength of the soil plays a critical role in the feasible design of offshore structures because dynamic loads on the structure can cause plastic deformation of the soil in extreme load cases. The shear strength is also considered as one of the dominant variables to determine the degradation of the shear modulus.

Shear strength τ_f linearly depends on the effective normal stresses σ' as

$$\tau_f = c + \sigma' \quad \tan\phi. \tag{5}$$

where c is the cohesion. When Mohr's circle is under the yield line expressed with Eq. (5), yield does not occur. In a three dimensional space, Mohr-Coulomb yield surfaces can be calculated as

$$(\overline{\sigma}'_1 + \overline{\sigma}'_3)\sin\phi + 2c \quad \cos\phi - (\overline{\sigma}'_1 - \overline{\sigma}'_3) = 0, \tag{6}$$

where $\overline{\sigma}'_1$ is the first principal stress, and $\overline{\sigma}'_3$ is the third principal stress.

Depending on the drain rate of the soil and the rate of the load, the soil can be deformed either in undrained conditions or in drained conditions. Because the effective stresses (which denote stresses acting on the soil particles) are different for each condition, one should be careful when determining the value of the effective stresses in Eqs. (5) and (6). The undrained condition is defined as a situation when the drain rate of the water is much slower than the rate of dynamic load. Due to this relatively slow drain rate, the load is transferred to the pore water pressure. Thus, the changes in the stress acting on the soil particles (i.e., effective stress) due to the dynamic load are small. As a result, the dynamic load is not able to change the soil microstructure significantly. Therefore, the effects of dynamic loads on the shear strength are assumed negligible, suggesting that the effective stresses in Eqs. (5) and (6) are stresses calculated by static loads only. The drained shear strength is defined as the strength when the drain rate of the water is much faster than the rate of dynamic load. As a result, the dynamic load is transferred to the soil particles. Because this behavior changes the soil microstructure, the shear strength increases over the dynamic load. Hence, Eqs. (5) and (6) should be used with stress values which consider static loads and dynamic loads.

To determine the proper condition (either undrained or drained) when pullout loads act on a suction caisson, Deng and Carter proposed a nondimensional parameter T_k [78] as

$$T_k = \frac{k_s}{v_F D_s m_v \gamma_w}, \tag{7}$$

where v_F is the rate of displacement induced by loads; D_s is the diameter of the suction caisson; m_v is the coefficient of one dimensional volume decrease; γ_w is the unit weight of pore water; k_s is the permeability of the soil. In case T_k is larger than 0.6, the soil can be considered as in the drained condition. In case T_k is less than 0.002, the undrained condition must be considered.

Several researchers have investigated the undrained shear strength for various vertical effective stresses (σ'_{vc}) caused by static loads, PI, and OCR. In laboratory tests, the value of undrained shear strength is linearly proportional to the vertical effective stress (σ'_{vc}) [79]. The ratio (S_u/σ'_{vc}) of normally consolidated silts and clays is about 0.2 for small PI (i.e., PI of less than 20%). The ratio increases over PI and becomes 0.25 when PI is larger than 80%. The effect of OCR on the undrained shear strength was suggested by Ladd [80,81] as $(S_u/\sigma'_{vc})_{OC} = (S_u/\sigma'_{vc})_{NC}OCR^{0.8}$, where $(S_u/\sigma'_{vc})_{OC}$ is the ratio of over-consolidated clay and $(S_u/\sigma'_{vc})_{NC}$ is the ratio of normally consolidated clay. Thus, the undrained shear strength can be estimated by using Eq. (8) as

$$S_u = \sigma'_{vc}(8.33\times10^{-4}(\mathrm{PI} - 20)+0.2)\mathrm{OCR}^{0.8}. \tag{8}$$

Due to the linear relation between S_u and σ'_{vc}, in situ experiments show that S_u linearly increases over the depth. Results obtained by Marchetti et al. [82] showed a shear strength profile of $S_u = 1.5z$ (kPa). For in situ tests on soft clays [83], S_u was measured as $1.125z$.

When the undrained shear strength profile ($S_u = S_u(z)$) for a site is provided, the shear strength in drained condition for that site can be calculated using the following procedure: 1) Calculate the vertical stress ($\sigma'_{vc} = \sigma'_{vc}(z)$) due to the weight of soil by integrating the unit weight from 0 to z; 2) Estimate the value of c and ϕ in Eq. (5) by using $S_u(z)$ and $\sigma'_{vc}(z)$; 3) Calculate the undrained shear strength by substituting c, ϕ, and the effective stress induced by the total load (i.e., dynamic and static loads) into Eq. (5).

3.4. Damping

The vibration energy of OWECs is dissipated by several damping sources [84]: hysteresis in the dynamic response of the soil, friction between the foundation and the soil, structural damping in the OWECs, aerodynamic damping, and hydrodynamic damping. Thus, all damping sources including soil damping are discussed in this section. The ranges of damping ratios of each source are provided also. The overall damping ratio for the first bending mode of OWECs is in the range of 2–3% [85–87].

Structural damping typically occurs when vibration energy is transformed into heat due to internal friction in a material. Det Norske Veritas (DNV) and Germanische Lloyd (GL) [84,88] calculated the structural damping ratio of a wind turbine structure by measuring the impulse response of the structure. The value is in the range of 1–1.5%, which includes both structural damping in the material and energy dissipation at joints. The aerodynamic damping of OWECs depends on the operational conditions. When the turbine is producing power, the aerodynamic damping ratio is between 0.08% and 0.5% [89–91]. This damping ratio decreases over the wind speed due to a reduction in the angle of incidence and the fast dynamics of the pitch control system [91]. The damping ratio decreases to 0.08% at stand-still conditions.

Hydrodynamic damping is caused by viscous hydrodynamic drag and wave radiation due to the vibration of the structure. The viscous damping is very small because the motion of offshore wind turbine structures is slow (low frequency). Damping ratio caused by wave radiation is approximately 0.12% for the first natural bending frequency of OWECs [92].

Soil damping is composed of hysteretic damping, friction damping, and radiation damping. When the height of the structure is much larger than its width, the effects of the radiation damping on the soil-structure interaction are significantly smaller than the effects of other damping [93]. Thus, studies on OWECs have been focused on hysteretic and friction damping. Friction damping is caused by the sliding on the surface where the foundation contacts the soil. Fakharian et al. [94] suggested that different criteria need to be used depending on the condition of drainage (i.e., either drained condition or undrained condition) when determining if sliding will occur. In drained conditions, they assumed that the structure starts to slide when the shear stress on the contact surface is larger than $0.3(c+K_o\sigma'_v\tan\phi)$. In undrained conditions, the sliding takes place when the shear stress on the contact surface is larger than $\alpha_s S_u$, where the value of nondimensional parameter α_s is between 0.22 and 0.28. When the shear strain of the soil is larger than $10^{-3\%}$, the hysteretic damping is considerable. This phenomenon is related to the changes of secant modulus over strain. In this range of shear strain, the shape of stress-strain curve is different for loading and unloading, as noted in Section 3.2. As the shear strain increases, the difference in the shape increases. Because the area of the hysteretic loop affects the hysteretic damping ratio (ζ_{hys}) [95], the damping ratio increases over the shear strain, as observed in several experiments [44,52,96,97]. Rollins et al. [96] proposed a hyperbolic curve to relate the damping ratio and shear strain as

$$\zeta_{hys} = 0.8 + 18(1 + 0.15\,\gamma^{-0.9})^{-0.75}. \quad (9)$$

The values of the various coefficients in Eq. (9) can change depending on the vertical stress and the PI because of their influence on the secant modulus, as mentioned in Section 3.2. Soil damping ratio was estimated by using the dynamic response of offshore wind turbines [85,86]. A soil damping ratio was calculated by subtracting the structural, aerodynamic and hydrodynamic damping from the overall damping ratio. The value obtained was in the range of 0.44–0.8%.

3.5. Degradation due to cyclic loads

The lifetime of an offshore structure strongly depends on the degradation of the soil shear modulus caused by cyclic loads. That is because the decrease of the shear modulus can lower the bearing capacity of the structure to extreme loads. Moreover, the decrease in shear modulus can shift the natural frequency of the structure close to the frequency range of the loads. It is noteworthy that a small amount of shift in the natural frequency can be critical for offshore structures. For example, a favorable 1st fore-after tower bending mode of (soft-stiff) offshore wind turbine is between the rotor speed frequency and three times the rotor speed frequency. This value is comparable to the frequency (i.e., about $0.2\,s^{-1}$) where the power spectrum of wave elevation is maximum [98]. Thus, the degradation of the soil shear modulus can cause significant vibrations.

Intensive experiments on the response of soil samples to cyclic loads have been performed by using strain- or stress- controlled cyclic loads. In strain-controlled cyclic load tests, harmonic (or similar to harmonic) cyclic strain with constant magnitude of the cyclic strain (γ_c) is applied to the soil samples. Then, the degradation of the shear modulus is calculated by measuring the magnitude of the shear stress (τ_{cN}). In stress-controlled cyclic load tests, the magnitude of strain (γ_{cN}) is observed when harmonic (or similar to harmonic) cyclic stress of constant amplitude (τ_c) is applied. The degradation index δ [55,99–101,107,112] is defined as

$$\delta = \frac{G_N}{G_1} = \begin{cases} \frac{\tau_{cN}/\gamma_c}{\tau_{c1}/\gamma_c} = \frac{\tau_{cN}}{\tau_{c1}}, & \text{for strain-controlled cyclic loads} \\ \frac{\tau_c/\gamma_{cN}}{\tau_c/\gamma_{c1}} = \frac{\gamma_{c1}}{\gamma_{cN}}, & \text{for stress-controlled cyclic loads} \end{cases}, \quad (10)$$

where N is the number of cycles; and G_N is the secant modulus at cycle N. The stress-controlled cyclic loads can cause faster degradation of the shear modulus because they apply larger strain energy to the soil than the strain-controlled cyclic loads. In strain-controlled experiments, the magnitude of stress decreases as the shear modulus reduces. Thus, the strain energy per cycle decreases over cycles. However, the magnitude of the shear strain increases with the degradation of the shear modulus when a constant magnitude of cyclic stress acts on the soil. As a result, the strain energy per cycle increases over the cycle.

When strain-controlled cyclic loads act on the soil, the changes of the degradation index δ over the cycle number can be estimated by using the degradation parameter t_D [55,99–101] as

$$\delta = N^{-t_D}. \quad (11)$$

If the soil shear modulus degrades quickly over N, the value of t_D is large. The degradation parameter t_D is a function of γ_c, OCR, σ'_{vc}, f_c, and PI, where f_c is the frequency of the cyclic strain. Table 8 presents the value of variables and corresponding t_D reported in several experiments [99–101]. It is observed that t_D increases with γ_c, σ'_{vc}, and f_c. Also, t_D is inversely proportional to OCR and PI. Values are sorted with γ_c, σ'_{vc}, and f_c in ascending order and sorted with OCR and PI in descending order so that Table 8 can reveal the dependency of t_D on variables more clearly.

In contrast to strain-controlled cyclic loads, it is difficult to obtain a unique empirical equation involving a single coefficient and able to

Table 8
Experimental conditions and estimated degradation parameter t_D in degradation experiments with strain-controlled cyclic loads.

γ_c (%)	OCR	σ'_{vc} (kPa)	f_c (Hz)	PI (%)	Test type[a]	t_D	Ref.
0.003	1	280	0.1–0.2	12	D	0.003	[101]
0.01	1	280	0.1–0.2	12	D	0.003	[101]
0.031	1	280	0.1–0.2	12	D	0.043	[101]
0.096	1	274	0.1–0.2	47	D	0.043	[101]
0.099	1	37	0.1–0.2	26	D	0.037	[101]
0.1	1	220	0.001	28	D	0.029	[100]
0.1	1	220	0.01	28	D	0.041	[100]
0.1	1	220	0.1	28	D	0.06	[100]
0.1	1	280	0.1–0.2	12	D	0.05	[101]
0.1	1	698	0.001	28	D	0.022	[100]
0.1	1	698	0.01	28	D	0.033	[100]
0.1	1	698	0.1	28	D	0.042	[100]
0.25	1	220	0.01	28	D	0.087	[100]
0.25	1	220	0.1	28	D	0.109	[100]
0.25	1	698	0.01	28	D	0.07	[100]
0.25	1	698	0.1	28	D	0.083	[100]
0.3	1	37	0.1–0.2	26	D	0.077	[101]
0.3	1	71.8	–	–	T	0.05	[55]
0.3	1	274	0.1–0.2	47	D	0.054	[101]
0.31	1	280	0.1–0.2	12	D	0.098	[101]
0.48	2	426	0.2	45	D	0.033	[99]
0.5	1	71.8	–	–	T	0.044	[55]
0.5	1	143.6	–	–	T	0.05	[55]
0.5	1	220	0.001	28	D	0.092	[100]
0.5	1	220	0.01	28	D	0.133	[100]
0.5	1	220	0.1	28	D	0.157	[100]
0.5	1	698	0.001	28	D	0.065	[100]
0.5	1	698	0.01	28	D	0.082	[100]
0.5	1	698	0.1	28	D	0.098	[100]
0.59	1	1392	0.2	45	D	0.047	[99]
0.64	4	353	0.2	45	D	0.038	[99]
0.74	1	71.8	–	–	T	0.068	[55]
0.83	1	37	0.1–0.2	26	D	0.104	[101]
0.99	4	415	0.2	45	D	0.03	[99]
0.99	2	478	0.2	45	D	0.048	[99]
1	1	71.8	–	–	T	0.052	[55]
1.04	1	280	0.1–0.2	12	D	0.176	[101]
1.49	1	1,162	0.2	45	D	0.079	[113]
1.5	1	71.8	–	–	T	0.129	[55]
1.5	1	143.6	–	–	T	0.137	[55]
1.74	4	355	0.2	45	D	0.043	[99]
2	1	71.8	–	–	T	0.184	[55]
3.48	1	274	0.1–0.2	47	D	0.292	[101]
5.09	1	475	0.2	45	D	0.159	[99]

[a] D denotes the direct shear test; and T denotes the triaxial shear test.

Table 9
Degradation experiments and experimental conditions; strain-controlled cyclic loads.

τ_c/S_u	τ_{av}/τ_c	OCR	PI (%)	f_c (Hz)	Test type	Ref.
0.24–0.72	0	1	–	0.01, 0.1, 1	D	[102]
0.3–0.85	0–7.15	1, 4, 40	27	0.1	T, D	[107]
0.14–0.83	0	1, 4, 10	–	0.1	D	[110]
0.1–0.4	1	1, 4, 10	–	0.1	T	[110]
0.2–0.9	0	1, 2, 3	–	0.01, 0.05, 0.1, 0.5, 1	T	[111]
0.26–0.56	1	1	28	0.05, 0.17, 0.83	T	[112]
0.3–0.6	0.5–2		27	0.1	S	[113]
0.12–0.37	0	1		0.1–4.9	T	[114]
0.25–0.85	0	1, 1.38, 2	21	0.1	S	[115]

estimate the results measured in various stress-controlled experiments. Therefore, instead of providing information such as degradation parameter t_D, Table 9 provides several stress-controlled experiments and their experimental conditions. When designing OWECs, one can effectively select the proper experimental data that has loading conditions and variables similar to the soil of the site by using Table 9.

Note that the mean value (τ_{av}) of the cyclic stress is not zero in some experiments. This nonzero mean value is necessary to predict the dynamic response of the foundation of OWECs. Because the thrust force acting on the nacelle of the wind turbine is considerable and its mean value is not zero, the stress acting on the soil will fluctuate with a nonzero mean value.

The degradation is faster for larger τ_c/S_u and τ_{av}/S_u in all experiments (Table 9). However, the effects of frequency and OCR are not consistent over experiments. Experiments performed by Ansal et al. [102] showed a very small effect of f_c between 0.1 and 1 Hz. Moreover, they observed that the degradation over N occurs slower for cyclic load with f_c of 0.01 than the degradation of f_c of 0.1 and 1 Hz. The effects of f_c are also not noticeable in experimental results obtained by Hyde et al. [103]. In contrast, slower loading rates cause faster degradation in other experiments [104–106]. High OCR increases the degradation rate in experiments performed by Andersen et al. [107]. However, Zhou et al. [112] reported opposite effects of OCR on the degradation. Effects of other properties (i.e., void ratio, unit weight, water contents, etc.) need to be considered to elucidate the effect of OCR and f_c on the degradation.

To secure reliability of OWECs, one should consider the degradation of the soil modulus when τ_c and τ_{av} stochastically change over cycles because the characteristics of the dynamic loads acting on OWECs vary over time. A theoretical approach to calculate the degradation induced by time-varying cyclic loads has been proposed [108,109]. However, the method requires the calculation of the accumulation of degradation per every cycle. Considering typical values of the first natural frequency of OWECs and their life span, OWECs should resist to a huge number of cyclic loads (of the order of 10^8). Thus, very intensive computational efforts are required when that method is used. To overcome this challenge, it is necessary to develop a novel method capable of predicting the long term-degradation caused by stochastically varying loads with fast computation.

4. Structure-soil interaction

4.1. Equivalent linear spring models

Soil-structure interaction can be considered by using equivalent soil stiffness when the structure interacts with a homogeneous soil and when the deformation of the soil is small so that the soil can be considered as linear material. The DNV code [88] suggests formulas for equivalent soil stiffness as

$$\begin{aligned}
k_V &= \frac{4GR}{1-\nu}\left(1+1.28\frac{R}{H}\right)\left(1+\frac{L}{2R}\right)\Bigg(1 \\
&\quad + (0.85-0.28\frac{L}{R})\frac{L/H}{1-L/H}\Bigg), \text{ for vertical stiffness,} \\
k_H &= \frac{8GR}{2-\nu}\left(1+\frac{R}{2H}\right)\left(1+\frac{2}{3}\frac{L}{R}\right)\left(1+\frac{5}{4}\frac{L}{H}\right), \text{ for horizontal stiffness,} \\
k_R &= \frac{8GR^3}{3(1-\nu)}\left(1+\frac{R}{6H}\right)\left(1+2\frac{L}{R}\right)\left(1+0.7\frac{L}{H}\right), \text{ for rocking stiffness,} \\
k_T &= \frac{16GR^3}{3}\left(1+\frac{8L}{3R}\right), \text{ for torsional stiffness,}
\end{aligned} \tag{12}$$

where R and L denote the radius and the length of the foundation. H is the thickness of the soil layer above the bedrock. Although one can simply obtain soil stiffness using this equation, this approach has several limitations. First, it is only applicable to pile-type foundations. Second, the DVN code notes that these formulas are valid when L is shorter than $2R$. This restriction cannot available to piles for OWECs in that most piles have very long length compare to their radius. Third, the bedrock should be located twice deeper than the length of piles to apply this equation. Hence, this equation is not useful when the bedrock is close to the piles. The reason for the many limitations of these formulas is that these formulas are originated from offshore gas and oil industries. The nature of the loads exerted onto OWECs and their geometry (including the overall size of their structures) are different. To overcome limitations of the DNV code, modified formulas, which are appropriate for OWECs, should be proposed.

Many studies have been conducted using lumped parameter models because of the simplicity of that approach. Adhikaria et al. [116,117] developed a wind turbine model composed of two lumped masses corresponding to wind turbine tower and nacelle. The mass corresponding to the tower was connected to a fixed boundary (i.e., soil) with a vertical spring and a rocking spring. Then, natural frequencies were calculated by solving the corresponding eigenvalue problem. This study showed that the first natural frequency significantly changed over the soil stiffness when the stiffness of soil was small, suggesting that the degradation of the soil modulus was dangerous especially when the soil was soft. This model was updated by Harte et al. [118]. They included viscous damping between the soil and the wind tower and between the wind tower and the nacelle. Sapountzakis et al. [119] connected an equivalent stiffness spring to the wind turbine tower modeled with a boundary element method. They showed that the structure with this equivalent stiffness had a first natural frequency 6% smaller than the natural frequency of the structure with a fixed boundary. Moreover, the response of the structure to earthquakes considerably increased when the equivalent stiffness was included between the tower and the boundary.

Lumped parameter models such as those based on equivalent spring models are beneficial because they can reduce the computation time and simplify equations of motions by considering the soil-structure interaction with a small number of linear springs. Furthermore, these models allow calculating analytical solutions or obtaining solutions with fast numerical formulas to predict the behavior of soil-foundation systems. However, these models have several important limitations. First, the value of the equivalent stiffness highly depends on the shape of the foundation. Thus, different values need to be obtained when using different shapes of foundation. Moreover, this method can provide a reliable result only if a site is composed of a homogeneous soil layer. If several soil layers are present around the structure, the predictions of these models may not be useful. Moreover, these models are incapable of considering the nonlinear behaviors such as the nonlinear stiffness of the soil and the gap that can be generated between the soil and the foundation. Despite these limitations, the equivalent linear spring models are useful for feasibility studies of particular sites and for conceptual design of OWECs for specific sites.

4.2. Distributed nonlinear spring models

To address the limitations of the equivalent linear spring model, the soil-structure interaction can be considered by distributing nonlinear springs on the soil-structure interface. The distributed springs can be characterized using load-deflection curves. The American Petroleum Institute (API) [120,121] provides several types of load-deflection curves which nonlinearly change over the lateral displacement (y) and the depth (z). These include p-y curves corresponding to lateral resistance, t-z curves corresponding to vertical resistance, and Q-z curves corresponding to bearing resistance, where p, t, and Q are the spring forces (which vary upon the soil properties and the magnitude of the y or z displacement of the structure). IEC 61400 [126], DNV and GL [84,88] also suggest the use of curves presented in the API code for the foundation design of OWECs [122]. These curves can be obtained by conducting in situ testing such as deflection of piles under lateral loads and the CPT [123,124]. If information on a candidate site is not accessible, the p-y curve for sand can also be approximated as [120]

$$p(y, z) = A(z)p_u(z)\tanh\left[\frac{kz}{A(z)p_u(z)}y\right], \tag{13}$$

where k denotes the modulus of subgrade reaction which can be obtained by applying a vertical load to a slab (which is on ground surface) and measuring its vertical deflection. The relation between k and the internal friction angle is shown in Fig. 6.8.7–1 of the API code [42]. The value of A can be evaluated as [42]

$$A = \begin{cases} 0.9 & \text{for cyclyc loading} \\ \left(3.0 - 0.8\frac{z}{D}\right) & \text{for static loading} \end{cases}, \tag{14}$$

Also, p_u is an ultimate bearing capacity, which can be determined as

$$p_u = \min\begin{Bmatrix} (C_1 z + C_2 D)\gamma' z \\ C_3 D\gamma' z \end{Bmatrix}. \tag{15}$$

The values of coefficients C_1, C_2, and C_3 are functions of the internal friction angle, as shown in Fig. 6.8.6–1 of the API code [120]. D denotes the pile diameter.

Several studies have been performed using distributed nonlinear springs for foundation modeling to predict the dynamic behavior of OWECs. Bisoi et al. [125] modeled a wind turbine tower and its foundation with Euler-Bernoulli beam elements. Distributed springs characterized by p-y, t-z, and Q-z curves were attached to the beam elements of the foundation. Then, aerodynamic and hydrodynamic loads were applied to the structure. The displacements of the OWEC when considering the soil-pile interaction were considerably larger compared to the displacements obtained when a fixed boundary condition is applied at the soil-structure interface. To study the effects of spatially varying soil properties, stochastic p-y curves [126] were proposed and integrated into a finite difference scheme to calculate the dynamic response of a monopile [127]. In these studies, the shear strength of the soil was stochastically changed over the depth. Because the stiffness of the soil depended on the shear strength, the stiffness of the soil also varied stochastically over the depth. Then, the first natural frequency of the structure was calculated. The results suggest that the natural frequency changes by 0.01–0.02 Hz due to stochastic variations in the soil strength. While these studies successfully showed the effects of uncertainty of soil properties on the natural frequency and on the displacement of structures, these studies could be enhanced by considering stochastic wind loads instead of quasi-static wind loads.

This distributed spring model was improved further to capture other soil-structure interaction phenomena such as the damping effects of soil and the separation of the soil from the structure in the presence of large loads. Gerolymos et al. [191] used laterally distributed translational springs and distributed rotational springs. A translational spring and a rotational spring were connected to the bottom of the structure. Then, the damping effect was considered by connecting distributed dashpots along with springs. Analytical expressions were derived for homogeneous and linear soils to predict the static and dynamic response. Then, this model was extended to study inhomogeneous and nonlinear soils [192]. This updated model can account for the effect of cyclic loads on separation and slippage at several conditions such as radiation damping, stiffness and strength degradation. This model was validated through experiments in medium-scale and a finite element analysis with a 3-D model [193]. Naggar et al. [128] differentiated the soil as soil adjacent to the structure and soil in the rest of the space. Each element of the pile was connected to the first layer of soil elements with springs and dashpots, and the first layer of soil elements was attached to the second layer of soil elements with different springs and dashpots. The first layer of soil elements captured the nonlinear stiffness of soil-structure interaction. The second layer of soil elements was used to account for the wave propagation through the soil. Then, the frequency responses were calculated for the lateral motion at the tip. Their predictions matched experimental data well, except for a small difference in the resonant frequency.

Distributed nonlinear spring models are more accurate than equivalent spring models because they can consider nonlinear mechanical properties of the soil and its spatial variability. However, elaborate studies are required to use such models because the nonlinear characteristics of the distributed springs vary upon the type of soils [194]. Moreover, these models require experiments to obtain parameters of the distributed stiffness. For example, the p-y curve should be obtained from in situ experiments of laterally loading piles installed in candidate sites and by measuring their deflection over the depth [194]. The p-y curve can be obtained also from laboratory tests by using soil samples [195]. Although distributed nonlinear spring models can successfully consider nonlinear interactions between the monopile and the soil, these models are difficult to apply for multipod foundations because the distributed springs should be modified to account for the interaction among piles through soil.

4.3. Continuum element models

Continuum element models of soil enable studies on complicated behaviors of soil-structure interaction that are difficult to consider using equivalent linear spring models or distributed nonlinear spring models. For example, continuum element models can predict the spatial distribution of variables (e.g., effective stress and pore water pressure) in two or three dimensions. Moreover, such models are useful to investigate multi-physical phenomena (e.g., interaction of mechanical stress, pore water pressure, and temperature) and interactions between suctions or piles when a multipod foundation is used for an OWEC.

Several constitutive models were proposed to account for the structural behavior of soils. They can be classified into the following: the linear elastic model, the nonlinear elastic model, the elasto-plastic model, the visco-elastic model, and the elasto-visco-plastic model [129]. Currently, the elasto-(perfectly) plastic model with the Mohr-Coulomb failure criterion (EPMC) is one of the most widely used models. This model assumes the yield surface is invariant over the plastic deformation. A nonlinear (hardening) elastic soil model [130] was developed from the hyperbolic elastic model. For unloading and reloading, different stress-strain relations are used. In this model, the yield surface can be expanded by plastic deformation. This model adopted distinct hardening rules to shear plastic strain and volumetric plastic strain. Lade [131] introduced various constitutive models along with their characteristic features on yield surface and on the parameter used to consider hardening.

Achmus et al. [132] predicted the behavior of piles under combined horizontal and vertical loading using EPMC. Based on numerous loading-displacement curves estimated from different loading conditions, they presented diagrams showing the relation of displacement of the pile and combined loads over different length and diameter of the

pile. These diagrams are useful to estimate equivalent stiffness of the piles if the effects of moments are included. Moreover, Abdel-Rahman et al. [133] compared the results obtained using EPMC for monopod foundations to the results obtained from *p-y* curves. This comparison suggested that *p-y* curves could underestimate the displacement of the piles. The effects of spatially nonhomogeneous soil on the behavior of the piles were also investigated. Haldar et al. [134] used soil with shear strength randomly varying over space with normal distribution. Then, the response of a pile to lateral loads was predicted. It was shown that the load capacity of a pile was enhanced when the strength distributes over the space more fairly.

Continuum element models can also be used to study the behavior of foundations under cyclic lateral loads induced by wind or waves. By using EPMC, Achmus et al. [135] calculated the accumulated plastic strain when lateral loads were exerted on the pile. Then, they predicted the degradation of the soil stiffness using an empirical equation correlating the decrease of the shear modulus to the plastic strain. Based on the results of parametric studies, relations of horizontal loads and displacements were proposed for both static and cyclic loading. Bourgeois et al. [136] simplified the earlier elasto-plastic models by assuming the effects of volumetric plastic strain were small. This assumption reduced the number of parameters, and hence models could be characterized with a relatively small number of tests (i.e., three monotonic tests and one cyclic triaxial test). Their experimental validation showed that the simplified models could predict the response of piles to monotonic loads. In addition, the model predictions for strain accumulation over the cycles of cyclic loads agreed reasonably well with experimental results. A hybrid foundation proposed in [137] consisted of an inside steel monopile and an outside lightweight steel footing. The footing needed to be filled with rubble after installation. In their study, the soil was modeled with the elastoplastic model with the Von Mises failure criterion. The associative flow rule was used to predict plastic deformation. It was predicted that the hybrid foundation provided higher stiffness than monopile foundations. The degradation of soil stiffness was also smaller for the hybrid foundation. The prediction of this study can be enhanced by capturing plasticity by using a Mohr-Coulomb, a modified Cam-Clay, or a soil hardening model because the Von Mises failure criterion does not consider the effects of the mean effective stress of soil on the shape of the yield surface.

To study the interaction between soil particles and water present among soil particles, multi-physical models based on the continuum elements have were developed. Cuéllar et al. [138] considered the behavior of structure to extreme loads (i.e., storms) by considering soil with a generalized plastic theory. Darcy's equation was coupled with the constitutive model of soil to predict the changes in the excessive pore water pressure over time. When the pile was vibrated by strong cyclic loads (caused by storms), the excessive pore water pressure near the pile and the lateral displacement of the structure were calculated. They also computed the response of the structure when the effect of excessive pore water pressure on soil was not considered. When this hydromechanical coupling effect was not included, the displacement was smaller than the displacement obtained from the coupled model by about 10–20%. This result suggested that the increase of pore water pressure decreased the effective stress, and thereby the resistance of the structure to loads was reduced. Dijkstra et al. [139] used a hypoplasticity soil model [140], which can account for the interaction of void ratio of soil and the stress distribution. The pore water pressure was also considered by using Darcy's law. Their results showed that changes in the stress and porosity were dominant within the region with a diameter of 3 times the pile diameter.

Continuum models predict nonlinear behaviors of soil and soil-structure interaction more accurately than equivalent or distributed spring models. Moreover, parameters of continuum models are less dependent on the design of the structure, while parameters of equivalent or distributed spring models vary with the shape and dimension of structures. Continuum models also can predict multi-physical behaviors, which are difficult to capture with equivalent or distributed spring models. For example, the interaction of pore water pressure and stress needs to be considered to predict the degradation of soil modulus. This interaction can be included in continuum models by using constitutive law of pore-elastic material [141–143]. However, predicting long-term degradation using continuum models is still challenge because these models require intensive computational efforts.

4.4. Experiments

4.4.1. Monotonic (and static) loading

Static responses of structure-soil interaction to single loads (e.g., lateral and vertical loads) were investigated for various soils types [144–150]. Based on these experimental results, several models were suggested to generate *p-y* curves [151]. More recently, the response of soil was investigated when several loads (e.g., vertical, lateral, and moment loads) acted on the structure at the same time. Experiments were conducted for structures installed in clay [152–154], dense sand [155–158], and loose carbonate sand [159,160]. These experiments provided useful empirical equations for yield curves of structure-soil system as functions of two combined loads. To extend these two-dimensional studies into three-dimensional models, the responses of footing structures to vertical, (two) lateral, torsional, and (two) rotating loads were measured. Then, a three dimensional yield surface [161,162] was suggested as

$$f = \left(\frac{h_2}{h_0}\right)^2 + \left(\frac{h_3}{h_0}\right)^2 + \left(\frac{m_2}{m_0}\right)^2 + \left(\frac{m_3}{m_0}\right)^2 - 2a\left(\frac{h_3 m_2 - h_2 m_3}{h_0 m_0}\right) + \left(\frac{q}{q_0}\right)^2 - \left(\frac{(\beta_1+\beta_2)^{(\beta_1+\beta_2)}}{\beta_1^{\beta_1}\beta_2^{\beta_2}}\right)^2 v^{2\beta_1}(1-v)^{2\beta_2} = 0, \tag{16}$$

where $h_2 = H_2/V_0$, $h_3 = H_3/V_0$, $m_2 = (M_2/2R)/V_0$, $m_3 = (M_3/2R)/V_0$, $q = (Q/2R)/V_0$, and $v = V/V_0$. h_0 denotes the normalized horizontal load capacity, m_0 denotes the normalized moment capacity, q_0 denotes the normalized torsional load capacity, a is the eccentricity of the ellipse in the $h - m$ plane, β_1 and β_2 are shaping parameters for the yield surface in the vertical load plane. V_0 denotes the intersection of the yield surface with the axis of the vertical load. A key contribution of this study is to determine allowable combinations of loads for the elastic response of the foundations. Load combinations within the surface result in elastic motion of the footing. If a load combination produces a value of f in Eq. (16) which is the same or larger than zero, then that load condition causes plastic deformation in the soil. Because this model focused on the failure due to static loads, extended studies to obtain response to cyclic and dynamic loads are necessary for OWECs.

4.4.2. Dynamic and cyclic loading

When cyclic lateral loads are exerted to structures, their deflections change over cycles. Effects of cyclic loads on the stiffness of soil are different for clay and sand because they have different permeability. The equivalent stiffness of the structure-soil systems can be calculated with the ratio of magnitudes of cyclic loads and corresponding displacement. It is worthy to note that the stiffness can be differently defined depending on whether the accumulated plastic deformations are included in the displacement. The stiffness obtained by using the total displacement (i.e., displacement including accumulated plastic deformations) is herein referred to as the plastic stiffness. When the accumulated plastic deformation is not considered, the ratio of cyclic loads over displacement is referred to as the cyclic stiffness.

For piles in clay, the cyclic stiffness degrades over the lateral cyclic loads. Due to the low permeability of clay, pore water pressures increase due to cyclic loads. This excessive pore water pressure can cause softening of clay [100,101]. Todd et al. [163] and Tuladhar et al. [164] observed the degradation of the cyclic stress in field tests. In their experiments, the accumulated plastic deformation was very small.

Experiments conducted by Lombardi et al. [165] showed the effects of cyclic loads on the natural frequency of OWECs. They measured the equivalent stiffness and the first natural frequency of 1/100 scale offshore wind turbines supported by a monopile in clay. The results showed that the natural frequency decreased over cyclic loads due to the degradation of the clay stiffness.

The cyclic stiffness of sand increases over the lateral cyclic loads acting on a pile. Because sand has high permeability, cyclic loads are transferred to the soil grains. Thus, loads can change the microstructure of sand. As mentioned in Section 3, the shear modulus of soil increases over the effective normal stress. Therefore, the cyclic stiffness of sand increases over cycles. However, the plastic stiffness decreases over cycles because the accumulated plastic deformation increases over cycles. Peng [166] obtained load-displacement curves by conducting laboratory cyclic load tests on small-scale piles. The cyclic stiffness increased over cycles, whereas the plastic stiffness decreased over cycles. Similar behaviors were observed in other studies also [123,167–169]. Various experimental results on accumulation of plastic deformation due to cyclic loads were in the study of Lin et al. [170]. Using existing results, they constructed an empirical equation to account for the effect of sand density and the pile installation method on the accumulation of plastic deformation. Both one-way and two-way cyclic loads were considered in the equation. Bhattacharya et al. [171] measured the equivalent stiffness and the first natural frequency of 1/100 scale offshore wind turbines supported by a monopile. Their results showed that cyclic loads increased the equivalent stiffness and natural frequency for dry and saturated sand. Several experiments demonstrated the mechanism of liquefaction under cyclic undrained loading conditions in loose to medium dense saturated sandy soil [172,173]. Liquefaction is critical to offshore structures as it decreases the soil stiffness near the structures.

4.5. Suction caissons

Details for theoretical and experimental efforts for suction caissons are separately discussed in this subsection because this type of foundation is the most cost-effective and promising solution for shallow waters and transitional depths waters. Suction caisson foundations were originally developed for oil and gas industry [174]. The technology for this foundation was introduced to floating platforms first, and applied to fixed platforms. The Draupner E is the first gas platform installed with a jacket suction substructure in the depths of 70 m [175–177], after performing large-scale penetration tests [178].

Many studies have been conducted to secure the reliability of OWEC foundations with suction caissons [179–183]. The first comprehensive investigation on the applicability of suction caisson for OWECs was presented by Byrne [184–186]. Then, several other studies have been reported, including laboratory model tests, and field trials using reduced-scale and full-scale structures [23].

4.5.1. Modeling for installation

A major difference of suction caissons from piles is the installation process (i.e., the additional forces induced from the suction pressure). The pressure difference causes flow of water within the soil and the (excessive) pore pressure gradients. This pressure difference is beneficial to the installation process because it can decrease the strength of soil around the caissons.

The installation of suction caissons has two phases: self-weight penetration and penetration induced by suction pressure. The self-weight penetration can be estimated by calculating the friction between the inside/outside of the caisson and the end bearing on the tip of the caisson. Then, negative suction pressure is applied to the caisson. The force balance in this second phase can be expressed for sand as [187]

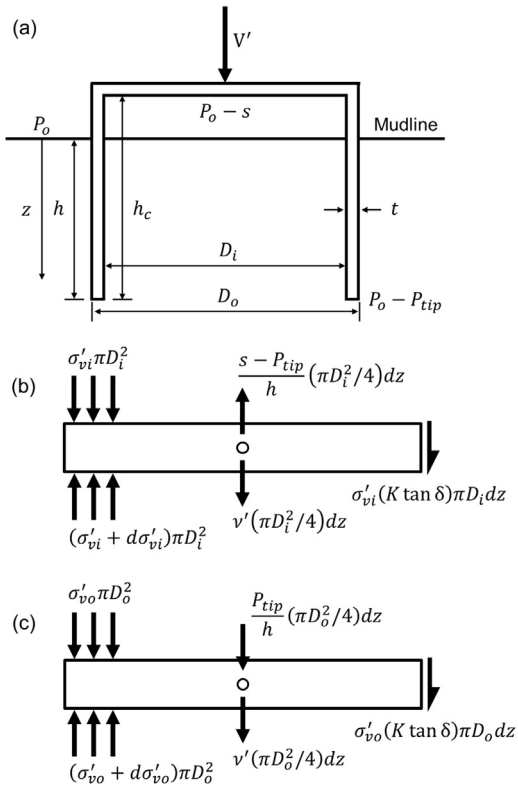

Fig. 9. (a) Outline of suction caisson: h and h_c denote the current embedment of the caisson and the height of the caisson. Vertical equilibrium of an infinitesimal horizontal slice of soil under stress (b) inside and (c) outside of the caisson.

$$V' + s\left(\frac{\pi D_i^2}{4}\right) = \int_0^h \sigma'_{vo} dz (K\tan\delta)_o(\pi D_o) + \int_0^h \sigma'_{vi} dz (K\tan\delta)_i(\pi D_i) + (\sigma'_{vi} N_q + \nu' t N_\nu)(\pi D t), \quad (17)$$

where V′, s, δ, D, D_i, D_o, t, N_q, N_ν, ν', K denote as follows: the vertical load caused by weight, the suction pressure within the caisson with respect to the ambient seabed water pressure P_o, the mobilized angle of friction between the suction skirt and soil, the mean diameter of the caisson, the inner diameter of the caisson, the outer diameter of the caisson, the thickness of the caisson, the overburden bearing capacity factor, the self-weight bearing capacity factor, the submerged unit weight of soil, and lateral earth pressure, respectively. Fig. 9 shows an outline of the suction caisson features. In Eq. (17), the first, the second, and the third terms on the right-hand side are the friction force acting on the outer surface, the friction force acting on the inner surface, the load bearing annulus, respectively. Friction forces are proportional to the normal forces acting on the suction skirt surface. The normal force corresponds to the horizontal effective stress on soil grains, which can be calculated as the product of K and the vertical effective stress adjacent to the caisson. Then, friction forces can be obtained by multiplying the mobilized friction angle δ to the normal force. The end bearing is obtained by the summing of the overburden bearing term and the self-weight bearing term (which is proportional to the area of the annulus).

To calculate the effective vertical stress inside and outside of the skirt, the excessive pressure gradient within the caisson and the tip of the caisson should be taken into account. An average upward pressure gradient (inside of the caisson) and downward pressure gradient (outside of the caisson) are $(s - P_{lip})/h$ and P_{lip}/h assuming that the distribution of pore water pressure on inside and outside of the caisson is linear over depth. Substituting P_{lip} to as results in $(s - as)/h$ for upward pressure gradient and as/h for downward pressure gradient, where a denotes the pressure factor. Note that the ambient seabed water

pressure should be larger than the pressure at the skirt, and the pressure at the skirt should be larger than the pressure inside of the caisson to create flow of water, i.e. $P_o > P_o - P_{tip} > P_o - s$. Considering these flows as well as the force induced to an infinitesimal horizontal slice of soil as shown in Fig. 9(b) and (c), the vertical stress equilibrium equations of the suction caisson become

$$\frac{d\sigma'_{vi}}{dz} - \sigma'_{vi}\frac{(K\tan\delta)}{\frac{D_i}{4}} = \nu' - \frac{s - P_{tip}}{h}, \quad \text{for inside}$$
$$\frac{d\sigma'_{vo}}{dz} - \sigma'_{vo}\frac{(K\tan\delta)}{\frac{D_o}{4}} = \nu' + \frac{P_{tip}}{h}, \quad \text{for outside} \tag{18}$$

Substituting $\frac{(K\tan\delta)}{D_i/4}$, $\frac{(K\tan\delta)}{D_o/4}$, $(s - P_{tip})/h$, and P_{tip}/h into Z_i, Z_o, $(s - as)/h$ and as/h, Eq. (18) becomes

$$\frac{d\sigma'_{vi}}{dz} - \frac{\sigma'_{vi}}{Z_i} = \nu' - \frac{s(1-a)}{h}, \quad \text{for inside}$$
$$\frac{d\sigma'_{vo}}{dz} - \frac{\sigma'_{vo}}{Z_o} = \nu' + \frac{as}{h}, \text{ for outside} \tag{19}$$

Equation (19) can be solved with boundary conditions given by $\sigma'_v = 0$ at z = 0, namely

$$\sigma'_{vi} = \left(\nu' - \frac{s(1-a)}{h}\right)\left(\exp\left(\frac{h}{Z_i}\right) - 1\right), \quad \text{for inside}$$
$$\sigma'_{vo} = \left(\nu' + \frac{as}{h}\right)\left(\exp\left(\frac{h}{Z_o}\right) - 1\right), \quad \text{for outside} \tag{20}$$

Integrating the vertical effect stress over depth leads to

$$\int_0^h \sigma'_{vi}dz = \left(\nu' - \frac{s(1-a)}{h}\right)Z_i^2\left[\exp\left(\frac{h}{Z_i}\right) - 1 - \left(\frac{h}{Z_i}\right)\right], \quad \text{for inside}$$
$$\int_0^h \sigma'_{vo}dz = \left(\nu' + \frac{sa}{h}\right)Z_o^2\left[\exp\left(\frac{h}{Z_o}\right) - 1 - \left(\frac{h}{Z_o}\right)\right], \quad \text{for outside} \tag{21}$$

Substituting Eq. (21) into Eq. (17) leads to

$$\begin{aligned} V' + s\left(\frac{\pi D_i^2}{4}\right) = {} & \left(\nu' + \frac{sa}{h}\right)Z_o^2\left[\exp\left(\frac{h}{Z_o}\right) - 1 - \left(\frac{h}{Z_o}\right)\right](K\tan\phi)_o(\pi D_o) \\ & + \left(\nu' - \frac{s(1-a)}{h}\right)Z_i^2\left[\exp\left(\frac{h}{Z_i}\right) - 1 - \left(\frac{h}{Z_i}\right)\right](K\tan\phi)_i(\pi D_i) \\ & + \left(\left(\nu' - \frac{s(1-a)}{h}\right)Z_i^2\left[\exp\left(\frac{h}{Z_i}\right) - 1 - \left(\frac{h}{Z_i}\right)\right]N_q \right. \\ & \left. + \nu' t N_\nu\right)(\pi Dt). \end{aligned} \tag{22}$$

The pressure factor a depends on the ratio of permeability for the soil inside and outside because sand within the caisson might become loose and thus exhibit higher permeability. Therefore, Houlsby et al. [187] suggested an empirical equation based on finite element analyses to accurately predict the pressure factor a. Moreover, they compared model predictions with several experiments.

The resistance to penetration in clay can be calculated in a similar way as [188]

$$V' + s\left(\frac{\pi D_i^2}{4}\right) = h\alpha_o s_{u1}(\pi D_o) + h\alpha_i s_{u1}(\pi D_i) + (\nu' h N_q + s_{u2}N_c)(\pi Dt), \tag{23}$$

where α_o, α_i, s_{u1}, s_{u2}, and N_c denote the adhesion factor for outside, the adhesion factor for inside, the average shear strength over the depth of the skirt, the shear strength at the tip of the caisson skirt, and the cohesion bearing capacity factor respectively. The shear strength is assumed to increase linearly with the depth, i.e. the shear strength $s_u = s_{uo} + b_s z$, where s_{uo} and b_s denote shear strength at mudline and a coefficient to consider linearly increasing shear strength over the depth. Therefore, the average shear strength between the mudline for a depth h is $s_{u1} = s_{uo} + b_s h/2$, and the shear strength at the tip of the caisson skirt is $s_{u2} = s_{uo} + b_s h$. The major difference in the model of suction penetration in the clay from the model regarding sand is that shear strength is unaffected by the effective vertical stress, whereas shear strength depends on vertical stress in sand. Houlsby and et al. [188] showed that these models were reliable by comparing model predictions with experiments.

Senders et al. [189] proposed a method to calculate the friction on the caisson skirt using the cone resistance profile obtained from the CPT. They assumed that the resistance on the tip and friction on the skirt linearly decreased over the suction pressure. This method was validated using data obtained from the centrifuge model test and data regarding suction caisson installations. They also investigated the suction installation in sand overlaid by clay [190]. They suggested applying two different models depending on the permeability of clay, suction pressure, and the pumping rate of the suction. When the permeability of clay was small, the suction pressure was considerable, and the pumping rate was fast; effects of clay plug were considered in their model.

4.5.2. Modeling for operation

Studies on the resistance of suction caissons under operation also have been carried out for various environmental conditions. The direction of loads acting on the suction caissons depends on the type of substructures. For monopod foundations, horizontal loads (H) and bending moments (M) are exerted to single suction caissons. For multipod and jacket foundations, vertical loads (V) also need to be considered.

The response of suction caissons to H and M loads is considered when they are connected to monopod foundations. Doherty et al. [196] investigated coefficients of six equivalent stiffness values (i.e., stiffness corresponding to one vertical, one torsional, two horizontal, and two moment loads) of a caisson embedded in elastic soil. They also considered the increase of the soil stiffness over the depth. Then, the coefficients were estimated by using results obtained from the continuum elements model of suction caissons. To apply the coefficients of stiffness for several conditions, the values of coefficients were calculated for various soil properties and caisson dimensions. Parametric studies conducted by Achmus et al. [197] showed the effects of suction caisson geometry, loading conditions, and soil properties on the motion of suction caissons. This study considered the behavior of soil using EPMC. When large horizontal loads were exerted to a structure, a caisson lid and soil were separated in their simulations. This phenomenon can degrade the bearing capacity of a suction caisson supporting an OWEC because the soil around the skirt of a caisson should resist to the whole load. Their study suggested that the ultimate capacity and the stiffness of the soil-suction systems strongly depended on the dimension of the caissons and the height where loads were exerted. Moreover, other methods were suggested with an upper bound plasticity formulation for estimating the lateral load capacity of suction caissons [198,199]. Experimental work [199] using a centrifuge showed that the proposed method was capable of estimating the load capacity.

The response of caissons to vertical tensile loads has been investigated to prevent caissons from pulling out. A phenomenological model was developed by Deng et al. [200] for the pull-out behavior of suction caissons. The model considered several failure modes (i.e., failures under undrained, partially drained, or fully drained condition), and the model was validated using experimental data and results obtained from finite element models. The proposed methods took into account the influence of the aspect ratio of the caisson, the internal friction angle of soil, the permeability of soil, and the loading rate. Moreover, parametric studies for the pull-out were also carried out with several variables [201]. The results suggested that the pull-out capacity increased linearly over soil cohesion values, and increased exponentially over the internal friction angle of the soil. However, the

effects of the Poisson's ratio and the dilatancy angles on the pullout strength were small. Achmus et al. [202,203] developed a multi-physical model considering pore water pressure and stress distribution in soil to capture tensile resistance of caissons in partially drained condition. They suggested that the geometry of caissons, soil characteristics, and loading conditions affected the tensile resistance of caissons. Interestingly, the tensile capacity had a strong correlation with the pullout rate. The mechanism of accumulated heave was also elucidated over cycle loads.

Studies on the behavior of caissons to combined loads (i.e., V, H, and M) are necessary for multipod or jacket foundations. Doherty et al., [204] calculated the frequency dependent impedances of suction caissons along vertical, horizontal, and rotational directions by using linear viscoelastic soil models. Then, they predicted that the stiffness of the soil-suction systems increased over the skirt length, and the stiffness increases over frequency. Kim et al. [205] studied bearing capacities of suction caissons attached to tripod foundations. A linear elastic perfectly plastic model with Tresca failure criterion was used to consider the behavior of clay. The vertical, horizontal, and moment bearing capacities of the tripod and the monopod configurations were compared. When a tripod foundation was used, the vertical and moment bearing capacities could be improved between 2 and 10 times, respectively, compared to caissons connected to monopods. Wu et al. [206] predicted the effects of cyclic loads on the bearing capacity by using linear elastic perfectly plastic soil models with Mises yield criterion. In their model, experimentally observed shear strength values [207] were used because experiments captured variations of shear strength over cyclic loads. The vertical, horizontal and moment bearing capacities decreased by 30–40% after 2000 cycles.

4.5.3. Experiments on installation

Several experimental studies on the installation of suction caissons have been carried out for sand and clay. Villalobos [208] experimentally showed astonishing penetration capability of suction caissons. He conducted installation tests in sand using small scale suction caissons with a diameter of 293 mm. In the absence of suction pressure, a vertical pressure of 25 kPa was required for 140 mm penetration. In the presence of suction pressure of 5 kPa, a vertical pressure of 1 kPa was enough to accomplish the same depth of penetration. Houlsby et al. [209] performed installation field tests with suction caissons with diameters of 1.5 and 3 m. For both caissons, a suction pressure of about 30 kPa was required to penetrate about 1 m.

More attention is needed in the presence of a clay or a silt layer because their low permeability decrease or block water flow among soil particles. This phenomenon was observed by Tran et al. [212,213] in suction installation tests at sites including silt layers. They observed peaks in the excessive pore water pressure versus penetration depth curve. If water flow in soil was impeded, upward gradients of excessive pore water pressure decreased. Then, the penetration ability of suction caissons degraded. Their numerical calculations also predicted that unstable inner-soil plug moved upward (up to 20% of the caisson penetration).

The high suction pressure induced by silt layers can create piping channels and soil overflow into the caisson. To prevent this dangerous event, a filtration method was developed by Wang et al. [214]. Their experimental results showed that the proposed filtration technique could reduce the volume of soil heave and prevent soil failure during installation in silts.

These experimental data can provide insight into suction penetration and useful information for design parameters. Specifically, non-dimensional metrics of suction performance give the designer insight into the relationship among design variables, soil properties, and penetration performances. The experimental penetration induced by suction pressure are summarized in Fig. 10; the penetration depth caused by the suction pressure and the weight of the suction caisson can be calculated from Eqs. (17) and (23). This figure is constructed with

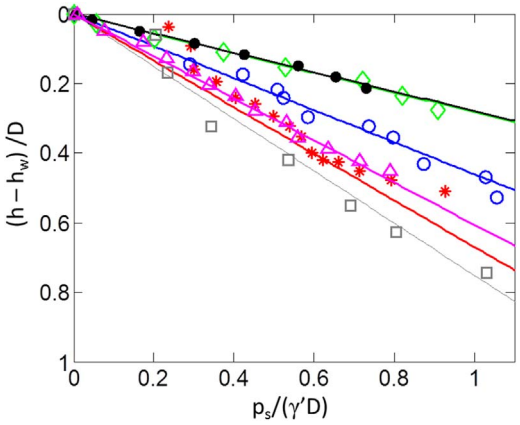

Fig. 10. Experimental results on penetration depth over suction pressure. h denotes the penetration depth of suction caissons, h_w is the penetration depth caused by the weight of the suction caissons, D is the diameter of the suction caissons, p_s is the suction pressure, and γ' is the submerged unit weight of soil. Parameter values corresponding to each symbol are provided in Table 10.

Table 10
Parameter values corresponding to the data shown in Fig. 10.

Symbol	D (m)	t (mm)	γ' (kN/m^3)	slope	Ref.
○	2	8	8.5	0.461	[187]
✳	4	20	8.5	0.671	[187]
◇	12	45	8.5	0.283	[187]
●	15	45	8.5	0.279	[187]
□	5.5	20	5.23	0.752	[190]
△	0.049	0.4	11	0.606	[210]

data from Refs. [187,190,210]. Each symbol represents different experimental results with different design variables at different sites (Table 10). The penetration performance of the suction caissons can be characterized by the slope of the lines by normalizing the penetration depth with respect to the diameter of the suction caisson and the suction pressure with the diameter of the suction caisson and submerged unit weight of soil. The penetration depth depends on the dimension of the suction caisson and the stiffness of the soil, suggesting that the slope has a strong dependence on soil properties and design variables (Table 10). Therefore, this normalization method can become an important metric to estimate the penetration performance in initial design steps because a large slope at the same soil conditions means an appropriate design.

4.5.4. Experiments on performance

The effects of the plasticity of soil on the behavior of suction caissons were observed in several studies. Villalobos et al. [215] measured the responses of small-scale caissons to monotonic loading in loose dry sand. Combined loads (i.e., V, H, and M) were exerted to their suction caissons and the corresponding displacements of the caissons were measured. Then, they calculated values of yield loads using obtained load-displacement curves. By connecting the yield loads, yield surfaces were established in the three-dimensional load space. They also built yield curves for caissons in saturated sand [216].

The behaviors of suction caissons under cyclic loads are of great interest. Byrne et al. [217] observed from laboratory tests that the stiffness did not change noticeably over the number of cycles. However, considerable degradation in the stiffness due to cyclic loads was observed in their field tests [209,218,219]. Cyclic moment loads and cyclic vertical loads were applied to suction caissons. For both these cyclic loads, high initial stiffness followed by hysteretic behavior was measured at moderate loads. Then, degradation of stiffness was observed when high loads were exerted on the caisson.

Cyclic loads can affect the static and dynamic characteristics of suction caissons. First, the position of suction caissons can be changed by cyclic loads. Wang et al. [220] observed that the suction caissons moved downward when the lateral cyclic load was larger than a critical value. This motion was larger if the cyclic load acted immediately after installation. Zhang et al. [221] applied asymmetric lateral cyclic loads to a suction caisson. They also observed a vertical and a horizontal motion of a suction caisson. They also observed that the motion was correlated over time to the excessive pore water pressure. Second, lateral cyclic loads can change the natural frequencies of OWECs. Bhattacharya et al. [222,223] developed a small scale offshore wind turbine with a monopod foundation with a single suction caisson. They installed the system in several different soils and applied large numbers of cyclic horizontal loads to the system by using a linear actuator. In the middle of the cyclic load testing, the natural frequency of bending mode was measured without a cyclic load. Then, cyclic loads were exerted to the wind turbine again. They repeated this procedure several times to measure the evolution of the natural frequency over cycles.

Other interesting experiments were also performed to study effects of caisson shape and loading rate on the behavior of suction caissons. The relationship between the pull-out loading rate and the tensile resistance was demonstrated with small scale model tests [224,225] and large scale suction caissons [226]. For the large-scale suction caissons, the tensile resistance increased over the rate of loading when the rate was between 0.83 and 3.33 N/s. However, the resistance remained almost the same if the loading rate was faster than 33.33 N/s. Kakasoltani et al. [224] studied the effects of the tilted angle of the skirt on its tensile resistances. They used upright suction caissons (i.e., tilted angle of skirt = 0°) and caissons with tilted angle of about 6°. They observed that the tensile resistance of the caissons with 6° titled angle was larger than that of upright caissons by 30–50%. Experiments also characterized the dependence of the pull-out resistance on the pull-out rate and the relative density of sand.

5. Future challenge and discussion

It is obvious that offshore wind energy has great potential. However, important progress and new approaches are required for successful development of offshore wind farms.

- General geotechnical standards, suggested by most guidelines for foundations of OWECs (API, DNV GL, IEC 61400), and semi-empirical models used in offshore wind were originally developed from offshore oil and gas industry. However, the nature of the loads exerted onto OWECs and the geometry (including the overall size of their structures) are different from load conditions of offshore oil and gas industry. Therefore, new experimental and theoretical studies specialized for OWECs are needed to modify current standards and semi-empirical models, which were developed based on conventional offshore structures. This attempt enables us to accurately predict static and dynamic responses of an OWEC coupled with a foundation and soil.
- In the authors' view, tripod and jacket structures with suction caissons are the most promising solution in the near future, whereas floating structures are competitive in the long run. Many countries such as the United States, China, Japan, and Korea have feasible wind resource potentials at sites where the water is deeper than 30 m. Tripod and jacket structures with suction caissons are effective solutions for these sites. For deeper seas, floating structures can be used effectively. Therefore, floating type foundations enable the use of the enormous ocean wind energy because oceans cover 71% of the Earth's surface and the wind speed in oceans is almost twice as large as that on land [227]. Hence, future research on OWECs should focus on developing new models for these types of foundations. Various demonstration projects with these foundations over the world currently support the need to develop elaborate models for those types of foundations.
- There is a lack of knowledge regarding the behavior of foundations and the degradation of soils under long-term cyclic loading. Especially, the study on the pullout mechanism of suction foundations under cyclic loading is still not sufficient to estimate structural stability and reliability accurately during service periods. Hence, the development of accurate degradation models and strain-accumulation models can provide valuable information to enhance the reliability and safety of OWECs.
- Operation and maintenance (O&M) is one of the critical issues in offshore wind energy considering the severe oceanic environmental conditions. From this perspective, corrosion and structural integrity of foundations are important to determine the lifespan of OWECs. Studies on novel fabrication and coating methods are required to enhance corrosion resistance and durability of materials for towers and foundations (as suggested by Arshad et al. [228]). Moreover, structural health monitoring systems are necessary to secure safety requirements and guarantee long term serviceability. Ultimately, online condition and structural health monitoring systems with powerful diagnosis and prognosis algorithms should be integrated with supervisory control and data acquisition (SCADA) systems. Based on these systems, cost-effective and condition-based maintenance decision strategies should be applied to O&M to minimize the downtime and thereby increase the commercial viability of offshore wind farms.
- Optimal methodologies for the construction of entire structures must be developed to minimize the cost and duration of tasks at offshore sites. A feasibility study on offshore wind farm including economic dynamics of the construction can also enhance the accuracy and decrease the uncertainty. Pantaleo et al. [229] quantified costs of foundations and offshore wind farms for the first time with several key factors such as the distance from shore, the water depth, the wind speed, the available area for wind farms, the cost for construction and O&M, and the electricity price. A variety of feasibility studies for offshore wind farms followed for different regions [5,6,230–233]. These analyses can be extended to comparisons of different foundation types with respect to costs and dynamic characteristics, and with respect to the economic dynamics of construction.
- The environmental impact of OWECs and foundations requires further investigations because issues such as noise and vibration caused during the installation of the foundation can be critical for fisheries. Hence, a deeper understanding of the dynamic response of foundations and innovative and ecologically friendly types of foundations will make offshore wind farms a more viable solution to the global energy challenge. These studies include noise and visual impacts [234,235], the effect of OWECs on marine animals and birds, and the effects of large scale OWECs on local climate [236].

Acknowledgements

This work was supported by the New & Renewable Energy Program of the Korea Institute of Energy Technology Evaluation and Planning (KETEP) grant funded by the Korean Government Ministry of Knowledge Economy (No. 20143010024330).

References

[1] Global wind report annual market update 2014. Available from: 〈http://www.gwec.net/wp-content/uploads/2015/03/GWEC_Global_Wind_2014_Report_LR.pdf〉.
[2] Achmus M, Wörden FT. Geotechnical aspects of the design of foundation structures for offshore wind energy converters. Bauingenieur 2013;43:157–65.
[3] The European offshore wind industry – key trends and statistics 2014. Available from: 〈http://www.ewea.org/fileadmin/files/library/publications/statistics/EWEA-European-Offshore-Statistics-2014.pdf〉.
[4] Zhixin W, Chuanwen J, Qian A, Chengmin W. The key technology of offshore wind farm and its new development in China. Renew Sustain Energy Rev

2009;13:216–22.
[5] Oh K-Y, Kim J-Y, Lee J-S, Ryu K-W. Wind resource assessment around Korean Peninsula for feasibility study on 100 MW class offshore wind farm. Renew Energy 2012;42:217–26.
[6] Oh K-Y, Kim J-Y, Lee J-K, Ryu M-S, Lee J-S. As assessment of wind energy potential at the demonstration offshore wind farm in Korea. Energy 2012;46:555–63.
[7] Crabtree CJ, Zappalá D, Hogg SI. Wind energy: UK experiences and offshore operational challenges. J Power Energy 2015;0:1–20.
[8] Musial W, Ram B. Large-scale offshore wind power in the United States – assessment of opportunities and barriers. NREL 2010. [TP-500-40745].
[9] Europe's onshore and offshore wind energy potential: an assessment of environmental and economic constraints. European Environment Agency. EEA Technical report No 6; 2009.
[10] Breton S-P, Moe G. Status, plans and technologies for offshore wind turbines in Europe and North America. Renew Energy 2009;34:646–54.
[11] Musial W, Butterfield S. Future for offshore wind energy in the United States. NREL 2004. [CP-500-36313].
[12] Mengé P, Gunst N. Gravity Based Foundations for the Wind Turbines on Thorntonback – Belgium. 15de Innovatieforum Geotechniek, Antwerpen, Belgium; 2008.
[13] Review of Options for Offshore Foundation Substructures Prepared by the Center for Wind Energy at James Madison University; 2012.
[14] 〈http://www.4coffshore.com/windfarms/〉.
[15] 〈https://en.wikipedia.org/wiki/List_of_offshore_wind_farms_in_Denmark〉.
[16] 〈https://en.wikipedia.org/wiki/List_of_offshore_wind_farms_in_Germany〉.
[17] 〈https://en.wikipedia.org/wiki/List_of_offshore_wind_farms_in_Sweden〉.
[18] 〈http://www.c-power.be/presentation〉.
[19] 〈https://en.wikipedia.org/wiki/List_of_offshore_wind_farms_in_the_Netherlands〉.
[20] 〈https://en.wikipedia.org/wiki/List_of_offshore_wind_farms_in_the_United_Kingdom〉.
[21] 〈https://en.wikipedia.org/wiki/List_of_offshore_wind_farms_in_China〉.
[22] 〈https://en.wikipedia.org/wiki/List_of_offshore_wind_farms_in_Japan〉.
[23] Oh K-O, Kim J-Y, Lee J-S. Preliminary evaluation of monopile foundation dimensions for an offshore wind turbine by analyzing hydrodynamic load in the frequency domain. Renew Energy 2013;54:211–8.
[24] Shi W, Han J, Kim C, Lee D, Shin H, Park H. Feasibility study of offshore wind turbine substructures for southwest offshore wind farm project in Korea. Renew Energy 2015;74:406–13.
[25] Ibsen LB, Liingaard M, Nielsen SA. Bucket Foundation, a status. Copenhagen, Denmark: Copenhagen offshore wind; 2005.
[26] Kim J-Y, Oh K-Y, Kang K-S, Lee J-S. Site selection of offshore wind farms around the Korean Peninsula through economic evaluation. Renew Energy 2013;54:189–95.
[27] Ryu MS, Kim J-Y, Kang K-S. The first met-mast for offshore wind farm in Korea and its remote sensing system. In: Proceedings of the twenty-first international offshore and polar engineering conference. Maui, USA; 2011, p. 511–5.
[28] Ryu MS, Kim J-Y, Lee J-S. Comparison of two meteorological tower foundations for offshore wind turbines. In: Proceedings of the twenty-sixth international offshore and polar engineering conference. Rhodes, Greece; 2016.
[29] Yang H, Zhu Y, Lu Q, Zhang J. Dynamic reliability based design optimization of the tripod sub-structure of offshore wind turbines. Renew Energy 2015;78:16–25.
[30] Lee Y-S, González JA, Lee JH, Kim YI, Park KC, Han S. Structural topology optimization of the transition piece for an offshore wind turbine with jacket foundation. Renew Energy 2016;85:1214–25.
[31] Jonkman JM, Buhl JrML. Loads analysis of a floating offshore wind turbine using fully coupled simulation. In: Proceedings of the wind power 2007 conference and exhibition. Los Angeles, USA; 2007.
[32] Jonkman JM, Buhl Jr. ML. Development and verification of a fully coupled simulator for offshore wind turbines. NREL 2007. [CP-500-40979].
[33] Nielsen FG, Hanson TD, Skaare B. Integrated dynamic analysis of floating offshore wind turbines. In: Proceedings of the 25th international conference on offshore mechanics and arctic engineering. Hamburg, Germany; 2006.
[34] Skaare B, Hanson TD, Nielsen FG. Importance of control strategies on fatigue life of floating wind turbines. In: Proceedings of the 26th International conference on offshore mechanics and arctic engineering. San Diego, USA; 2007.
[35] Myhr A, Maus KJ. The twenty-first international offshore and polar engineering conference. Maui, USA; 2011, p. 353–60.
[36] Shin H. Model test of the OC3-hywind floating offshore wind turbine. In: Proceedings of the twenty-first international offshore and polar engineering conference. Maui, USA; 2011, p. 361–6.
[37] Hanson TD, Skaare B, Yttervik R, Nielsen FG, Havmøller O. Comparison of measured and simulated responses at the first full scale floating wind turbine Hywind. Amsterdam, Netherland: EWEA Offshore; 2011.
[38] 〈http://www.statoil.com/en/TechnologyInnovation/NewEnergy/RenewablePowerProduction/Offshore/HywindScotland/Pages/default.aspx?RedirectShortUrl=http%3a%2f%2fwww.statoil.com%2fHywindScotland〉, [Accessed 13 November 2015].
[39] Yamamoto S, Colburn JrWE. Power generation assemblies and apparatus for use therewith. US 7293960 B2; 2007.
[40] Wayman EN, Sclavounos PD, Butterfield S, Jonkman J, Musial W. Coupled dynamic modeling of floating wind turbine systems. In: Proceedings of the offshore technology conference, Texas, USA; 2006.
[41] 〈http://www.fukushima-forward.jp/pdf/pamphlet3.pdf〉.
[42] Hunt RE. Geotechnical engineering investigation handbook. 2nd edition CRC Press; 2005.
[43] Tomlinson M, Woodward J. Pile design and construction practice. 5th edition CRC Press; 2008.
[44] Vucetic M, Dobry R. Effect of soil plasticity on cyclic response. J Geotech Eng 1991;117(1):89–107.
[45] Likitlersuang S, Teachavorasinskun S, Surarak C, Oh E, Balasubramaniam A. Small strain stiffness and stiffness degradation curve of Bangkok clays. Soils Found 2013;53(4):498–509.
[46] Diaz-Rodriguez JA, Lopez-Molina JA. Strain thresholds in soil dynamics. In: Proceedings of the 14th world conference on earthquake engineering; 2008, p. 12–7.
[47] Hardin BO. The nature of stress-strain behavior for soils. In: Proceedings of the ASCE geotechnical, Vol. 1. Engineering Division Specialty Conference on Earthquake Engineering and Soil Dynamics; 1978, p. 3–90.
[48] Hardin BO, Black WL. Vibration modulus of normally consolidated clay. J Soil Mech Found Div ASCE 1968;94(2):353–69.
[49] Seed HB, Idriss IM. Soil moduli and damping factors for dynamic response analyses [Report no. EERC 70-10]. Berkeley, California: Earthquake Engineering Research Center, University of California; 1970.
[50] Iwasaki T, Tatsuoka F, Takagi Y. Dynamic shear deformation properties of sand for wide strain range [Report of Civil Engineering Institute, No. 1085]. Tokyo, Japan: Ministry of Construction; 1976.
[51] Kagawa T. Moduli and damping factors of soft marine clays. J Geotech Eng 1992;118(9):1360–75.
[52] Seed HB, Wong RT, Idriss IM, Tokimatsu K. Moduli and damping factors for dynamic analyses of cohesionless soils. J Geotech Eng 1986;112(11):1016–32.
[53] Okur DV, Ansal A. Stiffness degradation of natural fine grained soils during cyclic loading. Soil Dyn Earthq Eng 2007;27(9):843–54.
[54] Assimaki D, Kausel E. An equivalent linear algorithm with frequency-and pressure-dependent moduli and damping for the seismic analysis of deep sites. Soil Dyn Earthq Eng 2002;22(9):959–65.
[55] Idriss IM, Dobry R, Doyle EH, Singh RD. Behavior of soft clays under earthquake loading conditions. In: Proceedings, eighth annual offshore technical conference. Dallas; 1976.
[56] Heshmati AA, Shahnazari H, Sarbaz H. The cyclic threshold shear strains in very dense clean sand. Eur J Environ Civ Eng 2015;19(7):884–99.
[57] Theenathayarl T. Behavior of sensitivity Leda clay under simple shear loading [Dissertation for the degree of Master of applied science in civil engineering]. University of Peradeniya; 2015.
[58] Shibata T, Soelarno DS. Stress-strain characteristics of sands under cyclic loading. Proc Jpn Soc Civ Eng 1975:239.
[59] Hardin BO, Drnevich VP. Shear modulus and damping in soils: design equations and curves. Soil Mech Pound Div, ASCE 1972;98(7):667–92.
[60] Pinto PA. Study of constitutive models for soils under cyclic loading [Dissertation for the degree of Master of Science in Civil Engineering]. Insitituto Superior Tecnico; 2012.
[61] Schneider JA, Hoyos L, Mayne PW, Macari EJ, Rix GJ. Field and laboratory measurements of dynamic shear modulus of piedmont residual soils. Geotech Spec Publ 1999;92:12–25.
[62] Yamamoto T, Trevorrow MV, Badiey M, Turgut A. Determination of the seabed porosity and shear modulus profiles using a gravity wave inversion. Geophys J Int 1989;98:173–82.
[63] Yamamoto T, Torii T. Seabed shear modulus profile inversion using surface gravity (water) wave-induced bottom motion. Geophys J Int 1986;85:413–31.
[64] Trevorrow M, Yamamoto T, Badiey M, Turgut A, Conner C. Experimental verification of sea-bed shear modulus profile inversions using surface gravity (water) wave-induced sea-bed motion. Geophys J Int 1988;93:419–36.
[65] Trevorrow M, Yamamoto T. Summary of marine sedimentary shear modulus and acoustic speed profile results using a gravity wave inversion technique. J Acoust Soc Am 1991;90:441–56.
[66] Badiey M, Yamamoto T, Turgut A, Bennett R, Conner C. Laboratory and in situ measurements of selected geoacoustic properties of carbonate sediments. J Acoust Soc Am 1988;84:689–96.
[67] Roberts HH, Cratsley DW, Whelan T. Stability of Mississippi Delta sediments as evaluated by analysis of structural features in sediment borings. In: Proceedings of the offshore technology conference; 1975.
[68] Gibson RE, Brown PT, Andrews KRF. Some results concerning displacements in a non-homogeneous elastic layer. Z fur Angew Math und Phys ZAMP 1971;22(5):855–64.
[69] Klein GK, Duraev AE. Consideration of the increase of the modulus of elasticity of soil with increase of depth when calculating beams on a homogeneous supporting soil. Power Technol Eng 1971;5(7):627–30.
[70] Gazetas G, Makris N. Dynamic pile-soil-pile interaction. Part I: analysis of axial vibration. Earthq Eng Struct Dyn 1991;20(2):115–32.
[71] Yokota K, Konno M. Dynamics Poisson's ratio of soil. In: Proceedings of the 7th world conference of earthquake engineering, Vol. 3. Istanbul; 1980, p. 475–8.
[72] 〈daveboore.com/daves_notes/daves_notes_on_poissons_ratio.pdf〉.
[73] Dutta TT, Saride S. Influence of shear strain on the Poisson's ratio of clean sands. Geotech Geol Eng 2016;34:1359–73.
[74] Schmertmann JH, Hartmann JP, Brown PR. Improved strain influence factor diagrams. ASCE J Geotech Eng Div 1978;104(8):1131–5.
[75] Terzaghi K, Peck RB, Mesri G. Soil mechanics in engineering practice. 3rd edition New York: John Wiley & Sons; 1996.
[76] Chowdhury I, Dasgupta SP. Dynamics of structure and foundation – a unified approach. CRC Press; 2008.
[77] Bowles JE. Foundation analysis and design. 5th edition England: McGraw-Hill; 1997.
[78] Deng W, Carter JP. A theoretical study of the vertical uplift capacity of suction

caissons. In: Proceedings of the 10th international offshore and polar engineering conference; 2002, p. 342–9.
[79] Ladd CC, DeGroot DJ. Recommended practice for soft ground site characterization: Arthur Casagrande lecture. I,: Proceedings of the 12th pan American conference on soil mechanics and geotechnical engineering; 2003.
[80] Ladd CC. Stress-deformation and strength characteristics, state of the art report. In: Proceedings of 9th ISFMFE, Vol. 4; 1977, p. 421–94.
[81] Kamei T, Iwasaki K. Evaluation of undrained shear strength of cohesive soils using a flat dilatometer. Soils Found 1995;35(2):111–6.
[82] Marchetti S. In situ tests by flat dilatometer. J Geotech Eng Div 1980;106:299–321.
[83] Randolph MF, House AR, Analysis of suction caisson capacity in clay. In: Proceedings of the offshore technology conference. Houston, USA; 2002, OTC 14236.
[84] Guideline for the Certification of Offshore Wind Turbines. GL; 2005.
[85] Damgaard M, Ibsen LB, Andersen LV, Andersen JKF. Natural frequency and damping estimation of an offshore wind turbine structure. In: Proceedings of the twenty-second (2012) international offshore and polar engineering conference. Rhodes, Greece; 2012, p. 300–7.
[86] Damgaard M, Ibsen LB, Andersen LV, Andersen JKF. Cross-wind modal properties of offshore wind turbines identified by full scale testing. J Wind Eng Ind Aerodyn 2013;116:94–108.
[87] Versteijlen WG, Metrikine AV, Hoving JS, Smid E, Vries WED. Estimation of the vibration decrement of an offshore wind turbine support structure caused by its interaction with soil. In: Proceedings of the EWEA offshore 2011 conference. Amsterdam, Netherlands; 2011.
[88] Design of offshore wind turbine structures, Offshore Standard DNV-OS-J101. DNV; 2011.
[89] James GH, Carne TG, Veers PS. J Sol Energy Eng 1996;118:190–3.
[90] Shirzadeh R, Devriendt C, Bidakhvidi MA, Guillaume P. Experimental and computational damping estimation of an offshore wind turbine on a monopile foundation. J Wind Eng Ind Aerodyn 2013;120:96–106.
[91] Kühn M. Dynamics and design optimization of offshore wind energy conversion systems [Report 2001.002]. DUWIND, Delft University Wind Energy Research Institute; 2001.
[92] Leblanc C, Tarp-Johansen NJ. Monopile in sand, stiffness and damping. In: Proceedings of the EWEA conference. Brussels; 2011.
[93] Ambrosini RD. Material damping vs. radiation damping in soil-structure interaction analysis. Comput Geotech 2006;33:86–92.
[94] Fakharian K, Iraji A. Numerical modeling of suction pile installation in Caspian Sea clay with effective and total stress analyses. Int J Offshore Polar Eng 2010;20(4):313–20.
[95] Lundgreen CC. Damping ratio for laterally loaded pile groups in fine grained soils and improved soils [Dissertation for the degree of Master]. Brigham Young University; 2010.
[96] Rollins KM, Evans MD, Diehl NB. Shear modulus and damping relationships for gravels. J Geotech Geoenviron Eng ASCE 1998;124(5):396–405.
[97] Zhang RD, Andrus, Juang CH. Normalized shear modulus and material damping ratio relationships. J Geotech Geoenviron Eng 2005;131(4):453–64.
[98] Hasselmann K, Barnett TP, Bouws E, Carlson H, Cartwright DE, Enke K, et al. Measurements of wind-wave growth and swell decay during the Joint North Sea Wave Project (JONSWAP), Technical report; 1973.
[99] Vucetic M, Dobry R. Degradation of marine clays under cyclic loading. J Geotech Eng 1988;114(2):133–49.
[100] Mortezaie AR, Vucetic M. Effect of frequency and vertical stress on cyclic degradation and pore water pressure in clay in the NGI simple shear device. J Geotech Geoenviron Eng 2013;139(10):1727–37.
[101] Tabata K, Vucetic M. Threshold shear strain for cyclic degradation of three clays. In: Proceedings of 5th international conference on recent advances in geotechnical earthquake engineering and soil dynamics. Missouri Univ. of Science and Technology, Rolla, MO; 2010.
[102] Ansal AM, Erken A. Undrained behavior of clay under cyclic shear stresses. J Geotech Eng 1989;115(7):968–83.
[103] Hyde AFL, Yasuhara K, Hirao K. Stability criteria for marine clay under one-way cyclic loading. J Geotech Eng ASCE 1993;119(11):1771–889.
[104] Matsui T, Ito T, Ohara H. Cyclic stress–strain history and shear characteristics of clay. J Geotech Eng Div 1980;106(GT10):1101–20.
[105] Procter DC, Khaffaf JH. Cyclic triaxial tests on remoulded clays. J Geotech Eng 1984;110(10):1431–45.
[106] Wang JH, Liu YF, Xing Y, Di HM. Estimation of undrained bearing capacity for offshore soft foundations with cyclic load. China Ocean Eng 1998;12(2):213–22.
[107] Andersen KH, Kleven A, Heien D. Cyclic soil data for design of gravity structures. J Geotech Eng 1988;114(5):517–39.
[108] Stewart HE. Permanent strains from cyclic variable-amplitude loadings. J Geotech Eng 1986;112(6):641–61.
[109] Lin S-S, Liao J-C. Permanent strains of piles in sand due to cyclic lateral loads. J Geotech Geoenviron Eng 1999;125:798–802.
[110] Andersen KH, Rosenbrand WF, Brown SF, Pool JH. Cyclic and static laboratory tests on Drammen clay. J Geotech Eng Div 1980;105(5):499–529.
[111] Moses GG, Rao SN, Rao PN. Undrained strength behaviour of a cemented marine clay under monotonic and cyclic loading. Ocean Eng 2003;30(14):1765–89.
[112] Zhou J, Gong X. Strain degradation of saturated clay under cyclic loading. Can Geotech J 2001;38(1):208–12.
[113] Goulois AM, Whitman RV, Hoeg K. Effects of sustained shear stresses on the cyclic degradation of clay. In: Chaney RC, Demars KR, editors. Strength testing of marine sediments: laboratory and in-situ strength measurements, 883. ASTM STP; 1985. p. 336–51.
[114] Rascol E. Cyclic properties of sand: dynamic behaviour for seismic applications [Dissertation]. École polytechnique fédérale de Lausanne; 2009.
[115] Azzouz AS, Malek AM, Baligh MM. Cyclic behavior of clays in undrained simple shear. J Geotech Eng 1989;115(5):637–57.
[116] Adhikaria S, Bhattacharya S. Vibration of wind-turbines considering soil-structure interaction. Wind Struct 2011;14(2):85–112.
[117] Adhikaria S, Bhattacharya S. Dynamic analysis of wind turbine towers on flexible foundations. Shock Vib 2012;19:37–56.
[118] Harte M, Basu B, Nielsen SRK. Dynamic analysis of wind turbines including soil-structure interaction. Eng Struct 2012;45:509–18.
[119] Sapountzakis EJ, Dikaros IC, Kampitsis AE, Koroneou AD. Nonlinear response of wind turbines under wind and seismic excitations with soil-structure interaction. J Comput Nonlinear Dyn 2016;10:041007.
[120] Recommended Practice for Planning, Designing and Constructing Fixed Offshore Platforms-Working Stress Design. API; 2003.
[121] Recommended Practice for Planning, Designing and Constructing Fixed Offshore Platforms-Load and Resistance Factor Design. API; 2003.
[122] IEC 61400-3 Wind turbines – Part 3: Design requirements for offshore wind turbines. IEC; 2009.
[123] Reese LC, Cox WR, Koop FD. Analysis of laterally loaded piles in sand. Offshore Technol Civ Eng Hall Fame Pap Early Years 1974:95–105.
[124] Johnson R, Parsons RL, Dapp S, Brown D. Soil characterization and p-y curve development for loess, Technical report; 2007.
[125] Bisoi S, Haldar S. Dynamic analysis of offshore wind turbine in clay considering soil-monopile-tower interaction. Soil Dyn Earthq Eng 2014;63:19–35.
[126] Low BK, Teh CI, Tang WH. Stochastic nonlinear p-y analysis of laterally loaded piles. In: Proceedings of the international conference on structural safety and reliability (ICOSSAR). Newport Beach, California; 2001, p. 17–22.
[127] Andersen LV, Vahdatirad MJ, Sichani MT, Sørensen JD. Natural frequencies of wind turbines on monopile foundations in clayey soils – a probabilistic approach. Comput Geotech 2012;43:1–11.
[128] Naggar MHE, Novak M. Nonlinear analysis for dynamic lateral pile response. Soil Dyn Earthq Eng 1996;15:233–44.
[129] Ti KS, Huat BBK, Noorzaei J, Jaafar MS, Sew GS. A review of basic soil constitutive models for geotechnical application. Electron J Geotech Eng 2009;14:1–18.
[130] Schanz T, Vermeer PA, Bonnier PG. The hardening soil model: formulation and verification. Beyond 2000 Comput Geotech 1999:281–96.
[131] Lade PV. Overview of constitutive models for soils. Soils Const Models Eval Sel Calibration 2005:1–34.
[132] Acumus M, Thieken K. On the behavior of piles in non-cohesive soil under combined horizontal and vertical loading. Acta Geotech 2010;5:199–210.
[133] Abdel-Rahman K, Achmus M. Finite element modelling of horizontally loaded monopile foundations for offshore wind energy converters in Germany. In: Proceedings of the international symposium on frontiers in offshore geotechnics. Taylor and Francis, Perth. 2005, p. 391–6.
[134] Haldar S, Babu GLS. Effect of soil spatial variability on the response of laterally loaded pile in undrained clay. Comput Geotech 2008;35(4):537–47.
[135] Achmus M, Kuo Y-S, Abdel-Rahman K. Behavior of monopile foundations under cyclic lateral load. Comput Geotech 2009;36:725–35.
[136] Bourgeois E, Rakotonindriana MHJ, Kouby AL, Mestat P, Serratrice JF. Three-dimensional modelling of the behavior of a pile subjected to cyclic lateral loading. Comput Geotech 2010;37:999–1007.
[137] Anastasopoulos I, Theofilou M. Hybrid foundation for offshore wind turbines: environmental and seismic loading. Soil Dyn Earthq Eng 2016;80:192–209.
[138] Cuéllar P, Mira P, Pastor M, Merodo JAF, Baeßler M, Rücker W. A numerical model for the transient analysis of offshore foundations under cyclic loading. Comput Geotech 2014;59:75–86.
[139] Dijkstra J, Broere W, Heeres OM. Numerical simulation of pile installation. Comput Geotech 2011;38:612–22.
[140] Gudehus G. A comprehensive constitutive equation for granular materials. Solid Found 1996;36:1–12.
[141] Biot MA. General theory of three-dimensional consolidation. J Appl Phys 1941;12(2):155–64.
[142] Biot MA. Theory of elasticity and consolidation for a porous anisotropic solid. J Appl Phys 1955;26(2):182–5.
[143] Biot MA. Mechanics of deformation and acoustic propagation in porous media. J Appl Phys 1962;33(4):1482–98.
[144] Skempton AW. The bearing capacity of clays. In: Proceedings of the building research congress. London, UK; 1951, p. 190–9.
[145] Reese LC, Cox WR, Kooper FD, Analysis of laterally-loaded piles in Sands. In: Proceedings of the offshore technology conference. Huston, Texas; 1974, OTC2080.
[146] Vesic AS. Analysis of ultimate loads of shallow foundations. J Soil Mech Found Div ASCE 1973;99(1):45–73.
[147] Vesic AS. Bearing capacity of shallow foundations. In: Foundation engineering handbook. New York: Van Nostrand.
[148] Berger E, Mahin SA, Pyke R. Simplified method for evaluating soil-pile structure interaction effects. In: Proceedings of the offshore technology conference. Huston, Texas; 1977, p. 589–98.
[149] Boulanger R, Curras C, Kutter B, Wilson D, Abghari A. Seismic soil-pile-structure interaction experiments and analyses. J Geotech Geoenviron Eng 1999;125(9):750–9.
[150] Wilson DW. Pile superstructure interaction in liquefiable sand and soft clay [Dissertation for Ph.D.]. Davis: University of California; 1998.
[151] Dash SR, Bhattacharya S, Blakeborough A, Hyodo M. P-Y curve to model lateral response of pile foundations in liquefied soils. In: Proceedings of the world

conference on earthquake engineering. Beijing, China; 2008.
[152] Martin CM. Physical and numerical modelling of offshore foundations under combined loads [Doctoral Dissertation]. United Kingdom: University of Oxford; 1994.
[153] Martin CM, Houlsby GT. Combined loading of spudcan foundations on clay: laboratory tests. Géotechnique 2000;50(4):325–38.
[154] Martin CM, Houlsby GT. Combined loading of spudcan foundations on clay: numerical modelling. Géotechnique 2001;51(8):687–700.
[155] Gottardi G, Butterfield R. On the bearing capacity of surface footings on sand under general planar loads. Soils Found 1993;33(3):68–79.
[156] Gottardi G, Houlsby GT, Butterfield R. Plastic response of circular footings on sand under general planar loading. Géotechnique 1999;49(4):453–69.
[157] Cassidy MJ. Non-linear analysis of jack-up structures subjected to random waves [Doctoral Dissertation]. United Kingdom: University of Oxford; 1999.
[158] Houlsby GT, Cassidy MJ. A plasticity model for the behaviour of footings on sand under combined loading. Géotechnique 2002;52(2):117–29.
[159] Byrne BW, Houlsby GT. Observations of footing behaviour on loose carbonate sands. Géotechnique 2001;51(5):463–6.
[160] Cassidy MJ, Bienen B. Three-dimensional numerical analysis of jack-up structures on sand. In: Proceedings of the international offshore and polar engineering conference. Kitakyushu, Japan; 2002, p. 807–14.
[161] Byrne BW, Cassidy MJ. Investigating the response of offshore foundations in soft clay soils. In: Proceedings of the international conference on offshore mechanics and arctic Engineering. Oslo, Norway; 2002, OAME2002-28057.
[162] Bienen B, Byrne BW, Houlsby GT, Cassidy MJ. Investigating six-degree-of-freedom loading of shallow foundations on sand. Géotechnique 2006;56(6):367–79.
[163] Dunnavant TW, O'Neill MW. Experimental p-y model for submerged, stiff clay. J Geotech Eng 1989;115:95–114.
[164] Tuladhar R, Maki T, Mutsuyoshi H. Cyclic behavior of laterally loaded concrete piles embedded into cohesive soil. Earthq Eng Struct Dyn 2008;37:43–59.
[165] Lombardi D, Bhattachary S, Wood DM. Dynamic soil- structure interaction of monopile supported wind turbines in cohesive soil. Soil Dyn Earthq Eng 2013;49:165–80.
[166] Peng JR. Behaviour of finned piles in sand under lateral loading [Ph.D. Dissertation]. 2006.
[167] Long JH, Vanneste G. Effects of cyclic lateral loads on piles in sand. J Geotech Eng 1994;120(1):225–44.
[168] Little RL, Briaud JL. Full scale cyclic lateral load tests on six single piles in sand. Misc. Paper GL-88-27. College Station: Gentechnical Division, Texas A&M University.
[169] Long JH, Vanneste G. Effects of cyclic lateral loads on piles in sand. J Geotech Eng ASCE 1994;120(1):225–44.
[170] Lin S-S, Liao J-C. Permanent strains of piles in sand due to cyclic lateral loads. J Geotech Geoenviron Eng 1999;125:798–802.
[171] Bhattacharya S, Adhikari S. Experimental validation of soil–structure interaction of offshore wind turbines. Soil Dyn Earthq Eng 2011;31:805–16.
[172] Bhattachary S, Madabhushi SPG, Bolton MD. An alternative mechanism of pile failure in liquefiable deposits during earthquakes. Géotechnique 2004;54(3):203–13.
[173] Martin GR, Finn WDL, Seed HB. Fundamentals of liquefaction under cyclic loading. J Geotech Geoenviron Eng 1975:101.
[174] Senpere D, Auvergne GA. Suction anchor piles – a proven alternative to driving or drilling. In: Proceedings of the offshore technology conference. Houston, USA; 1982, OTC 4206.
[175] Tjelta TI. Geotechnical aspects of bucket foundations replacing piles for the Europipe-E jacket. In: Proceedings of the offshore technology conference. Houston, USA; 1994, OTC 7379.
[176] Bye A, Erbrich C, Rognlien B. Geotechnical design of bucket foundations. In: Proceedings of the offshore technology conference. Houston, USA; 1995, OTC 7793.
[177] Tjelta TI. Geotechnical experience from the installation of the Europipe jacket with bucket foundations. In: Proceedings of the offshore technology conference. Houston, USA; 1995, OTC 7795.
[178] Tjelta TI, Guttormsen TR, Hermstad J. Large-scale penetration test at a deepwater site. In: Proceedings of the offshore technology conference. Houston, USA; 1986, OTC 5103.
[179] House AR, Randolph MF, Borbas ME. Limiting aspect ratio for suction caisson installation in clay. In: Proceedings of the international offshore and polar engineering Conference. Brest, France; 1999, p. 676–83.
[180] Erbrich CT, Tjelta TI. Installation of bucket foundations and suction caissons in sand – geotechnical performance. Houston, USA; 1999, OTC 10990.
[181] El-Gharbawy S, Olson R. Modeling of suction caisson foundations. In: Proceedings of the international offshore and polar engineering conference; 2000, p. 670–7.
[182] Al-Khafaji Z, Audibert JME, Hossain MK, Templeton JS, Clukey EC. Suction caisson foundation design for vortex-induced vibration loading. In: Proceedings of the offshore technology conference. Houston, USA; 2003, OTC 15239.
[183] Fakharian K, Iraji A. Numerical modeling of suction pile installation in Caspian sea clay with effective and total stress analyses. Int J Offshore Polar Eng 2010;20(4):1–8.
[184] Byrne BW. Investigations of suction caissons in dense sand [Dissertation for Ph.D.]. United Kingdom: University of Oxford; 2000.
[185] Houlsby GT, Byrne BW. Suction caisson foundations for offshore wind turbines and anemometer mast. Wind Eng 2000;24(4):249–55.
[186] Byrne BW, Houlsby GT, Martin C, Fish P. Suction caisson foundations for offshore wind turbines. Wind Eng 2002;26(3):145–55.
[187] Houlsby GT, Byrne BW. Design procedures for installation of suction caissons in sand. Geotech Eng 2005;158:135–44.
[188] Houlsby GT, Byrne BW. Design procedures for installation of suction caissons in clay and other materials. Geotech Eng 2005;158:75–82.
[189] Senders M, Randolph MF. CPT-based method for the installation of suction caissons in sand. J Geotech Geoenviron Eng 2009;135:14–25.
[190] Senders M, Randolph M, Gaudin C. Theory for the installation of suction caissons in sand overlaid by clay. In: Proceedings of the international offshore site investigation and geotechnics conference. London, UK; 2007, p. 429–38.
[191] Gerolymos N, Gazetas G. Winkler model for lateral response of rigid caisson foundations in linear soil. Soil Dyn Earthq Eng 2006;26:347–61.
[192] Gerolymos N, Gazetas G. Development of Winkler model for static and dynamic response of caisson foundations with soil and interface nonlinearities. Soil Dyn Earthq Eng 2006;26:363–76.
[193] Gerolymos N, Gazetas G. Static and dynamic response of massive caisson foundations with soil and interface nonlinearities-validation and results. Soil Dyn Earthq Eng 2006;26:377–94.
[194] Pando MA. Analyses of lateral loaded piles with p-y curves – observations on the effect of pile flexural stiffness and cyclic loading. In: Proceedings of the Geo3 T2 conference, 3B-1-A49; 2013.
[195] Johnson R, Parsons RL, Dapp S, Brown D. Soil characterization and p-y curve development for loess [Report no. K-TRAN: KU-05-03]. 2007.
[196] Doherty JP, Houlsby GT, Deeks AJ. Stiffness of flexible caisson foundations embedded in nonhomogeneous elastic soil. J Geotech Geoenviron Eng 2005;131(12):1498–508.
[197] Achmus M, Akdag CT, Thieken K. Load-bearing behavior of suction bucket foundations in sand. Appl Ocean Res 2013;43:157–65.
[198] Aubeny CP, Han SW, Murff JD. Inclined load capacity of suction caissons. Int J Numer Anal Methods Geomech 2003;27:1235–54.
[199] Zhang JH, Chen ZY, Li F. Three dimensional limit analysis of suction bucket foundations. Ocean Eng 2010;37:790–9.
[200] Deng W, Carter JP. A theoretical study of the vertical uplift capacity of suction caissons. Int J Offshore Polar Eng 2002;12(2):89–97.
[201] Zeinoddini M, Nabipour M. A parametric study on the pull-out response of suction caissons. J Mar Eng 2009;5(9):1/E–16/E.
[202] Thieken K, Achmus M, Schröder C. On the behavior of suction buckets in sand under tensile loads. Comput Geotech 2014;60:88–100.
[203] Achmus M, Thieken K. Numerical simulation of the tensile resistance of suction buckets in sand. J Ocean Wind Energy 2014;1(4):231–9.
[204] Liingaard M, Andersen L, Ibsen LB. Impedance of flexible suction caissons. Earthq Eng Struct Dyn 2007;36:2249–71.
[205] Kim S-R, Hung LC, Oh M. Group effect on bearing capacities of tripod bucket foundations in undrained clay. Ocean Eng 2014;79:1–9.
[206] Wu K, Ma M, Chen R. Numerical analysis of cyclic bearing capacity of suction bucket foundation based on elasto-plastic FEM. Electron J Geotech Eng 2010;15:1–13.
[207] Wang J, Li C, Moran K. Cyclic undrained behavior of soft clays and cyclic bearing capacity of a single bucket foundation. In: Proceedings of the fifteenth international offshore and polar engineering conference; 2005.
[208] Villalobos F. Installation of suction caissons in sand. In: Proceedings of the chilean conference of geotechnics (Congreso Chileno de Geotecnia); 2007.
[209] Houlsby GT, Kelly RB, Huxtable J, Byrne BW. Field trials of suction caissons in sand for offshore wind turbine foundations. Géotechnique 2006;56(1):3–10.
[210] Erbrich C, Hefer P. Installation of the Laminaria suction piles? A case history. In: Proceedings of the offshore technology conference; 2002.
[212] Tran MN, Randolph MF, Airey DW. Installation of suction caissons in sand with silt layers. J Geotech Geoenviron Eng ASCE 2007;133(10):1183–91.
[213] Tran MN, Randolph MF. Variation of suction pressure during caisson installation in sand. Géotechnique 2008;58(1):1–11.
[214] Wang L, Yu L, Guo Z, Wang Z. Seepage induced soil failure and its mitigation during suction caisson installation in silt. J Offshore Mech Arct Eng 2014;136. [011103-1–011103-11].
[215] Villalobos FA, Byrne BW, Houlsby GT. An experimental study of the drained capacity of suction caisson foundations under monotonic loading for offshore applications. Soils Found 2009;49:477–88.
[216] Villalobos FA, Byrne BW, Houlsby GT. Moment loading of caissons installed in saturated sand. In: Proceedings of the international symposium on frontiers in geotechnics, ISFOG. University of Western; 2005, p. 411–6.
[217] Byrne BW, Houlsby GT. Experimental investigations of the response of suction caissons to transient combined loading. J Geotech Geoenviron Eng 2004;130:240–53.
[218] Byrne BW, Houlsby GT. Assessing novel foundation options for offshore wind turbines. In: Proceedings of the world maritime technology conference. London, UK; 2006.
[219] Houlsby GT, Kelly RB, Huxtable J, Byrne BW. Field trials of suction caissons in clay for offshore wind turbine foundations. Géotechnique 2005;55(4):287–96.
[220] Wang Y, Lu X, Wang S, Shi Z. The response of bucket foundation under horizontal dynamic loading. Ocean Eng 2006;33:964–73.
[221] Zhang JH, Zhang LM, Lu XB. Centrifuge modeling of suction bucket foundations for platforms under ice-sheet-induced cyclic lateral loadings. Ocean Eng 2007;34:1069–79.
[222] Bhattacharya S, Nikitas N, Garnsey J, Alexander NA, Cox J, Lombardi D, et al. Observed dynamic soil-structure interaction in scale testing of offshore wind turbine foundations. Soil Dyn Earthq Eng 2013;54:47–60.
[223] Bhattacharya S, Cox J, Lombardi D. Dynamics of offshore wind turbines on two types of foundations. Proc Inst Civ Eng: Geotech Eng 2013.
[224] Kakasoltani S, Zeinoddini M, Abdi MR, Arabzadeh H. An experimental

investigation into the pull-out capacity of suction caissions in sand. In: OMAE 2011. Rotterdam, Netherland; 2011, 49038.
[225] Feld T. Suction buckets, a new innovative foundation concept, applied to offshore wind turbines [Ph.D. thesis]. Aalborg: Aalborg University; 2001.
[226] Zhu B, Kong D-Q, Tong J-G, Kong L-G, Chen R-P. Model tests on penetration and pullout of suction caissons in silt. Chin J Geotech Eng 2011;33(7):1045–53. [in Chinese].
[227] Archer CL, Jacobson MZ. Evaluation of global wind power. J Geophys Res 2005;110:D12110.
[228] Arshad M, O'Kelly BC. Offshore wind-turbine structures: a review. Proc Inst Civ Eng – Energy 2013;166(4):139–52.
[229] Pantaleo A, Pellerano A, Ruggiero F, Trovato M. Feasibility study of off-shore wind farms: an application to Puglia region. Sol Energy 2005;79(3):321–31.
[230] Mostafaeipour A. Feasibility study of offshore wind turbine installation in Iran compared with the world. Renew Sustain Energy Rev 2010;14(7):1722–43.
[231] Lim HC, Jeong TY. Wind energy estimation of the Wol-Ryong coastal region. Energy 2010;35(12):4700–9.
[232] Mekhilef S, Safari A, Chandrasegaran D. Feasibility study of off-shore wind farms in Malaysia. Energy Educ Sci Technol Part A-Energy Sci Res 2012;29(1):519–30.
[233] Gao X, Yang H, Lu L. Study on offshore wind power potential and wind farm optimization in Hong Kong. Appl Energy 2014;130:519–31.
[234] Lee S, Kim K, Choi W. Annoyance caused by amplitude modulation of wind turbine noise. Noise Control Eng J 2011;59(1):38–46.
[235] Pedersen E. Health aspects associated with wind turbine noise. results from three field studies. Noise Control Eng J 2011;59(1):47–53.
[236] Keith DW, Joseph F, Denkenberger DC, Lenschow DH, Malushev SL. The influence of large-scale wind power on global climate. Proc Natl Acad Sci USA 2004;101(46):16115.